DR JINCHENG DU (Orcid ID : 0000-0003-4805-7498)

Article type : Article

Interfacial structures of spinel crystals with borosilicate nuclear waste glasses from molecular dynamics simulations

Wei Sun, Jincheng Du*

Department of Materials Science and Engineering, University of North Texas, Denton, Texas USA

(* Corresponding author. Email: du@unt.edu)

Abstract

Spinel crystal formation presents a critical issue in processing nuclear waste glasses and affects the waste loading and glass formulation. In this paper, the interfacial structures of the model borosilicate nuclear waste glasses, the international simple glass (ISG), with two types of spinel crystals, namely the $MgAl_2O_4$ and $NiFe_2O_4$, were studied using classical molecular dynamics simulations with effective partial charge potentials and recently developed composition-dependent boron related parameters. The simulation results revealed the structural features of the borosilicate nuclear waste glasses and their interfaces with the two types of spinel crystals. It was found that there exist notable structural changes of glasses close to the interface region, affected by the adjacent crystal structures, in terms of preferential segregation and

ordering of cations. Specifically, the fraction of four-fold coordinated boron (B_4) is different between the ISG bulk and the interface regions, resulting from the local structure change and ordering due to interface formation. In addition, the amount of four-fold coordinated Al decreases while five-fold Al increases in the glass region close to the glass-crystal interface, which suggests indication of initial stage of crystal growth as Al adopts higher (six-fold) coordination in the crystal as compared to majority of four-fold coordination in the glass. These interfacial structure changes obtained from MD simulations provide evidence of the influence of the precipitated crystals on the surrounding melt and glass which lead to the initial stage of crystal growth.

1. Introduction

Nuclear wastes generated from the nuclear energy industry and defense nuclear material production in the past eight decades have become significant international environmental and safety challenges. Development of ways to safely dispose these wastes is critical to address both the energy and environment issues of our era[1]. Vitrification, i.e. immobilize nuclear wastes in glass matrixes, is one of the most efficient and accepted way for treating these radioactive wastes, especially those with high and medium level radiactivity[2]. Borosilicate glasses are the widely accepted glass composition for immobilizing radioactive waste since these glasses have relatively low melting temperature and high long term chemical durability, as compared to conventional silicate glasses, which can effectively lower the risk of losing radionuclides during melting and subsequent storage[1, 3, 4]. During the processing of nuclear waste glasses, due to complex chemistry of the waste materials, crystalline phases can form and some poses serious issues in processing. For example, the formation of nepheline crystals in waste glasses is detrimental to the chemical durability due to consuming glass forming SiO_2 and Al_2O_3 during crystal formation[5,6]. Iron nickel ($NiFe_2O_4$) spinel crystal is another types of crystals that can form during the vitrification process and present a serious issue. These spinel crystals have high melting temperature and higher density than the melt, as a result they could block the melter discharge channels. It is thus critical, while designing nuclear waste glass composition, to develop a comprehensive understanding of the interactions of these spinel crystals with glass and melts. With these knowledge, glass composition or forming processes can be developed to avoid

or levitate the issues caused by these spinel crystals. The detailed knowledge of crystal formation and crystal/glass interfacial structures is also of general importance in glass science to understand crystallization behaviors and development of glass ceramics[7].

International simple glass (ISG) is considered to be a reference aluminoborosilicate nuclear waste glass and has been widely studied in past few years[8]. The structures of ISG are complicated due to interactions of six-oxide compositions, especially among the three glass formers, SiO_2, B_2O_3, and Al_2O_3, which lead to the mixed glass former effect[9]. Boron and aluminum ions can enter the three-dimensional [SiO_4] networks by replacing Si. Al^{3+} is mostly four-fold and forming [AlO_4] tetrahedra. Each [AlO_4]$^-$ tetrahedron, unlike [SiO_4], contains a negative charge, which needs to be compensated by cations charge compensators such as Na^+ or Ca^{2+} within ISG. As for B^{3+}, it can take three- and four-fold coordination state, existing as trigonal [BO_3] or [BO_4] tetrahedra, respectively[10]. The conversion process between the two boron oxidation states can be described by a two-state statistical model with different enthalpy[11]. Similar to Al^{3+}, [BO_4]$^-$ contains one negative charge and needs to be charge compensated by alkali and alkaline-earth cations in ISG. In addition, the structural features especially the fraction of 3- and 4-fold coordinated boron, namely N_3 and N_4 respectively, can alter with glass composition in aluminoborosilicate glasses. In ISG, the glass modifier oxides can play multiple roles such as charge compensator of four-fold coordinated boron, or generation of NBOs on [SiO_4] tetrahedra [12,13]. For example, it has been proposed that the Ca^{2+} causes formation of more NBOs than Na^+ due to its higher field strength[10], whereas the Na^+ mainly acts as a charge compensator[10].

The spinel structure with face-centered cubic lattice generally has a formula of AB_2O_4, in which A and B occupy the tetrahedral and octahedral interstitial sites of oxygen closed packed lattice, respectively. In this study, we chose two typical spinel structures, $MgAl_2O_4$ and $NiFe_2O_4$ to study the ISG-spinel glass/crystal interfaces. The divalent Mg^{2+} and Ni^{2+} in these two spinel crystals occupy the tetrahedral sites with a coordination number of four, whereas the trivalent cations Al^{3+} and Fe^{3+} have coordination number of six, occupying octahedral sites. These two spinel structures have been widely studied on both experimental and theoretical studies. However, the lack of detailed atomic structural information clouds the understanding and further application of ISG glass. Although experimental characterizations such as nuclear magnetic resonance (NMR) can provided information on the structure of ISG glass (such as cation-anion

distances), the obtained highly complex signals make it difficult to determine the detailed structures[1].

Classical molecular dynamics (MD) simulations can provide systematic studies on short and medium range structures in multi-oxide glasses [14–17], as well as the glass/crystal interfaces. Collin *et al.*[2] reported MD simulations on pristine ISG and the results were validated by experimental data. Garofalini et al. reported a series of MD simulations regarding the silica and alumina, including structures of silica/alumina interfaces[18], calcium silicate/alumina interfaces[19], and calcium-alumino-silicate glasses/alumina interfaces[20,21]. Recently, Jiang and Garofalini reported a MD study on intergranular glassy films (IGFs) on growth of the prism surface in β-Si_3N_4[22]. Rushton et al.[4] reported interfaces between sodium lithium borosilicate glasses and the MgO and CaO crystals and found that the borate and silicate polyhedral shows strong correlation on position and orientation[4]. We have recently reported the interfacial behaviors between soda magnesia aluminosilicate glass and $MgAl_2O_4$ spinel crystals and found that that aluminum ions changed from mainly 4-fold coordination in the glass to 5 and 6-fold coordination near the interface[23]. This provides evidence of the influence of the crystal structure on that of the glass at the interface, which can be an initial stage of crystal growth. Recently, Deng and Du[24] has developed as set of composition dependent boron potentials that are compatible with the existing potentials that allow simulations of full compositions of ISG.

The aim of this work is to investigate the structure properties of ISG glasses and interfaces between ISG and spinel ($MgAl_2O_4$ and $NiFe_2O_4$) crystals using molecular dynamics simulations with the newly developed boron potential parameters. The atomic distribution within the interfaces were studied using z-density profiles, pair distribution function, bond angle distribution and other analysis methods to gain insights of the local structure change or ordering at the crystal-glass interface, as well as the effect of the types of crystals on these kind of ordering behaviors.

This paper is organized as follows: the next section describes the simulation methodology from empirical potential, to glass formation procedure, to interface building procedure and structural analysis methods. The results section first reports the structure of ISG glass from simulation and then ISG-spinel interfacial structures of two types low energy spinel surfaces: (110) and (111) for the two spinel crystals. Then the ordering of cations around the glass/crystal interfaces were summarized. This is followed by discussions and conclusions.

2. Computational Details

To validate the empirical potentials used in the MD simulations, the structure and mechanical properties of the related spinel structures was first calculated using the energy minimization method implemented in the General Utility Lattice Program (GULP) package[25]. And for the glass formation and construction of the interface models, classical molecular dynamics simulations were performed by using the DL_POLY package. Partial charge pair-wise potentials were employed to describe the partial covalent and partial ionic nature of the chemical bonding in the glass and crystal structures. The short-range interaction is in the Buckingham form:

$$V_{ij}(r_{ij}) = A_{ij}\exp\left(-\frac{r_{ij}}{\rho_{ij}}\right) - \frac{C_{ij}}{{r_{ij}}^6} \quad (1)$$

where *r* represents the interatomic distance; *A, ρ,* and *C* are the parameters for the Buckingham term. In order to avoid the overriding of the power term to the exponential term that caused problems at high temperature and initial high energy configurations at the interface. A splice function was thus introduced to correct the original Buckingham potential at short interatomic distancdes[26]:

$$V'(r_{ij}) = B_{ij}{r_{ij}}^2 + D_{ij}{r_{ij}}^n \quad (2)$$

where B, D and n are parameters chosen to ensure the potential, force and first derivative of force to be continuous at the splicing distance r_s. The partial atomic charge and parameters for short range interactions are listed in Table 1[27]. Boron related parameters were recently developed and has a composition dependent A_{ij} parameter for B-O interactions to account for the effect of glass composition on boron coordination change[26]. Details of the potential development and testing can be found in Ref. 27.

As a validation of the potentials, calculations of the bulk spinel $MgAl_2O_4$ and $NiFe_2O_4$ were performed and the properties of the two oxides were calculated and compared with reported experimental data and first principles density functional theory (DFT) data. The Bulk, Shear, and Young's moduli were calculated based on the elastic moduli components c_{ij} according to the Voigt-Reuss-Hill scheme[28,29]. The experimental crystal structures, as well as mechanical

properties from experimental measurements and from first principles calculations were also included in Table 2 and 3 for comparison. It can be seen that the adopted empirical potentials were able to reproduce the structures of both $MgAl_2O_4$ and $NiFe_2O_4$ spinel very well. The elastic moduli components, Bulk moduli, and Shear moduli were also very well reproduced by the potential. However, the Young's moduli from calculations were lower than experimental values for both crystals. This might be due to the calculated Young's modulus is an isotropic estimation from the Voigt-Reuss-Hill scheme while experimental values can be anisotropic. This difference can also be due to large variations in reported mechanical properties such Bulk and Young's moduli caused by sample and measurement conditions. In addition, the set of potential in Table 1 has been applied to ISG as well as several aluminonsilicate glass systems[30–32] and been proved to successfully predict the complex glass structure, thermal and mechanical properties. Hence the choice of the comprehensive set of potential is due to its capability to describe both the crystal and glass phases, as well as its transferability to describe glasses in wide composition ranges. It is expected that the potentials can hand complex interfacial structures and behaviors.

Slab models with applied three-dimensional periodic boundary condition were adopted to create the crystal surfaces and crystal/glass interfaces. The starting configuration for interface calculations consists of the ISG layer and spinel crystal surface layer, in which the supercell models for spinel $MgAl_2O_4$ and $NiFe_2O_4$ (100), (110), and (111) surfaces were generated. In addition, for both of the two crystals, the as-cleaved (111) surface are not suitable for interface generating and analyzing since the cut-plane's shape is not rectangular. Therefore, the redefined $MgAl_2O_4$ and $NiFe_2O_4$ (111) surfaces were performed by constructing orthogonal surface vectors as depicted in Figure 1. The final dimensions of as-cleaved $MgAl_2O_4$ (100), (110), and (111) surfaces for interface building are *40.25Å×40.25Å×28.5Å*, *40.45Å×34.32Å×28.8Å*, and *45.77Å×39.64Å×37.05Å*, respectively. For $NiFe_2O_4$ (100), (110), and (111) surfaces, the dimensions are *41.81Å×41.81Å×75.9Å*, *41.81Å×47.31Å×44.15Å*, and *40.97Å×47.31Å×47.60Å*, respectively.

Table 4 shows the ISG glass composition. To build an interface, the initial *x* and *y* dimensions of simulation cell were determined by the size of the $MgAl_2O_4$ and $NiFe_2O_4$ surface cells. Since three chosen crystal surface slabs, (100), (110), and (111) have different dimensions,

three glasses with different cell sizes for each crystal were generated with the different sets of *x* and *y*. The *z* dimensions of glass cells were chosen accordingly to keep the density and total number of atoms consistency. The three initial glass systems were generated containing around 6000 atoms with the same composition by randomly placing all the atoms in the corresponding cells. This was followed by heating to 6000 K using constant volume (NVT) simulations, and then quenching down to 300 K gradually with a cooling rate of 5K/ps. The final glass structures were then used to form interface together with cleaved crystal supercell.

Figure 2 shows the schematic structure of initial generated $MgAl_2O_4$(110)/ISG interface model. The interface was created by insertion of $MgAl_2O_4$ crystal part and glass part, with a 5 Å gap between both of the sides. The initial interface was then melted at 6000 K followed by a step by step quench process to 300 K. Figure 3 shows the schematic temperature profile of the MD simulation process of interface formation in this work. It can be seen that two cooling stages were taken places in the quench process. From 6000 K to 1000K, the system was first relaxed at 6000 K for 50 ps, and then cooled down to 1000 K at a cooling rate of 5 K/ps with constant volume calculations in the canonical (NVT) ensemble. It is worth mention that the atomic positions in the crystalline component were fixed during this state, otherwise the crystalline phase could melt down into liquid ceramic phase. The second state started from 1000 K to 300 K, in which all atoms positions were allowed to relax since the temperature range is far below the melting temperature of spinel $MgAl_2O_4$. In addition, to allow volume relaxation of the simulated systems, subsequent MD calculations were performed in the isobaric, isothermal (NPT) ensemble and NVE ensemble in which simulation cell dimensions are allowed to vary with time.

The parital total correlation function (TDF, named T(r) in the figures) and bond angle distribution (BAD) analyses were used to study the atomic structures of ISG and interfaces. The TDF and BAD analyses were averaged over 600 configurations in the final state of the production run (NVE ensemble) in duration of 50 ps at 300 K. To characterize the interface structure and atom distribution, z-density profile along with Coordination number (CN) profile were performed for the final relaxed structures.

The z-density profile (ZDP) analysis were used to study the composition changes along the dierection perpendicular to the crystal-glass interface. ZDP plots were constructed as follows: the

system was subdivided into a series of slices parallel to the interface, each with a *z* dimension of 0.2 Å or 0.5 Å. The number of atoms in each slice was then calculated in each of the slices. This number was then divided by the volume of the slice to obtain atom number density.

3. Results

3.1 General structure features of ISG

The short-range structures of glasses can be effectively described by using pair distribution functions such as partial total correlation functions (T(r)) and bond angle distributions. Figure 4 shows the simulated partial TDF along with the coordination distribution for ISG. The bond distance of an atom pair is represented by the first peak position in their partial correlation functions. For some pairs, for example B-O, there exist two peaks which represent two different bond distances that correspond two coordination states. For Si-O pair, the main peak is at 1.61 Å, which agrees well with reported boroaluminosilicate[33], ISG[2] and aluminosilicate glasses from MD[30] results and X-ray absorption spectra results from experiments[34]. The main peak of Al-O pair, which is also considered as a glass former, locates at 1.75 Å, in a good agreement with previous MD simulation results of sodium aluminosilicate glasses[30], as well as the experimental conducted XRD and EXAFS of both alumina and sodium-aluminosilicate glasses[35,36]. For another significant glass former, B-O pair distribution plot contains two main peaks indicated in Figure 4. The first peak locates at around 1.46 Å, corresponding to three-coordinated boron (B^3), while the second peak locates at around 1.52 Å, corresponding to four-coordinated boron (B^4). Interestingly, the bond distance of B-O pair and B^3/B^4 ratio are highly depended on boron concentration[24]. For the glass modifier in this system, Na-O, Ca-O and Zr-O pairs display broader peaks, locating at around 2.47 Å, 2.40 Å, and 2.10 Å, respectively, which agrees with previous results[27].

The bottom panel of Figure 4 shows accumulated coordination number of ISG. Both Si and Al are found to be four-fold coordinated, which agrees with previous MD studies for ISG[2]. Different from Si, the coordination number of Al depends on the glass composition. Xiang *et al.* [30] reported that when the composition with Al/Na ratio is one or smaller than one, Al ions are mainly four-coordinated. As the Al/Na ratio increases, the five-coordinated Al accordingly increases and four-coordinated Al decreases. In ISG, it is alkali rich hence Al exist in four-fold coordination. It is worth mentioning that Al ions usually exists in six-fold coordinated in oxides

crystals, such as in $MgAl_2O_4$ spinel and Al_2O_3 corundum structures. For B in ISG, the average coordination number is around 3.5, which indicates around 50% of B are four-coordinated in ISG. As found in this study, the formation of the glass-crystal interface can influence the Al and B coordination.

Usually, O-Si-O BAD are used to describe the regularity of the silicon oxygen tetrahedrons, whereas the Si-O-Si BAD represent the tetrahedron connectivity. It can be seen in Figure 5 that the O-Si-O bond BAD shows a peak at around 108°, which is in agreement with the experimental data based on neutron and high-energy X-ray diffraction[37]. This result is consistent with theoretical angle of tetrahedral, indicating the SiO4 polyhedron. The peak of O-Al-O BAD, shown in Figure 5b, is relatively wider than that of O-Si-O and locates at around 107°, which agrees well with previous simulation results in sodium-aluminosilicate and boro-aluminosilicate glasses. While for O-B-O, the bond angle is slightly wider than O-Si-O, locating at around 109°. Additional structure features of ISG[2] and ISG with different amount of ZrO_2[38] were reported elsewhere.

3.2 Structures of $MgAl_2O_4$(110)/ISG interfaces

The schematic structures of the side view of local configuration of ions near both AlO-terminated and MgAlO-terminated (110)/ISG interface were demonstrated in Figure 6. The dashed lines indicate the outer layer of $MgAl_2O_4$ crystal, separating the atoms from the glass and the crystal. The colors assigned to each type of atom are consistent with the ones in z-density profile plots. In Figure 6, large orange atoms represent B species from glass. For better demonstrating B species, only B-O bonds are showed in this and following figures. It can be seen that some B atoms from the glass were absorbed onto both AlO-terminated and MgAlO-terminated sides, forming bonds with the O atoms from glass and the outer layer of crystal. In addition, some Al atoms from glass segregate to the crystal surface and form bonds with O from crystal.

The segregation of B and Al showed in Figure 6 in glass were then verified by Z-density profiles (ZDP) of the (110) interfaces, along with other elements. ZDP analyses were used to study the elemental distribution perpendicular to the crystal-glass interface. For ZDPs shown in Figs. 7, 10, 12 and 14, the contributions from the spinel crystal were not included to focus on the

change of the glass structure due to the interface formation and the ZDP were calculated at 0.5 Å intervals. For ZDPs in Figs. 8, 11, 13, 15, the analyses were done at a higher resolution at 0.2 Å in order to examine details of structure changes at the crystal-glass interface. And in these figures, both the crystal and glass contributions are shown.

Figure 7 shows the atomic density profiles for (110)/glass interface. It is found that the intensity of O, Si, Al, and Ca are higher near both AlO- and MgAlO-terminated sides of the crystal part, indicating an ordering of these species segregated from ISG. The intensity of these peaks decrease accordingly when moving further into the glass, where the center of the glass reaches the normal glass density. In addition, different magnitudes of decay for different peaks are observed in Figure 7. For B, Zr, and Ca the density maxima closed to the crystal surface are generally much larger than the rest of the glass. While the peaks of O and Si species decay gradually from crystal surface to glass bulk. It is worth mention that the Al peaks at MgAlO-terminated side are higher than those at AlO-terminated side. According to the orientation of (110) surface with a sequence of …AlO–AlMgO-AlO-AlMgO…, the next layer after AlMgO denotes to AlO layer, which leads to the segregation of Al from ISG.

In Figure 8, high definition z-density profiles including both crystal (dashed lines) and glass (solid lines) within about 10 Å near both sides of interface are plotted, in order to take a close investigation of atoms distribution. It can be seen in Figure 8a that the stronger peak of O species from glass overlapping with relatively smaller Si and B peaks were absorbed into the AlO-terminated (110) surface. The peaks of B and Al decay to a low lever into glass bulk direction. Interestingly, small peaks of O from crystal can be observed at glass side, locating at about 1 Å above the outer layer of AlO-terminated surface.

Different distribution is observed near MgAlO-terminated side. In Figure 8b, overlapping of O, B, and Al originating from ISG are observed near the surface, following by the relatively high Si peak overlapping with B and O. Although the location of O feature appearing in ISG side is closer to the crystal surface than that at AlO-terminated side, the “movement: of O atoms from crystal to ISG after quench down to 300K is still exist, indicating the ion exchange between glass and crystal to some extent.

3.3 Structures of $MgAl_2O_4$(111)/ISG interfaces

The $MgAl_2O_4$ (111) surface, with layer stacking sequence of ・・・anion-cation-anion-cation・・・, has a much higher net dipole moment along surface normal direction. Therefore, such high polarity results in quite different atoms segregations from ISG. The schematic structures of side view of local configuration of ions at two terminated (111)/ISG interface models after melt-quench process are demonstrated in Figure 9. The (111) surface used in construction of interface model contains O-termination on one side and Al-termination on the other side. Similar to (110)/ISG models, the dashed line represents the outer Al and O layer of Al-terminated and O-terminated (111), respectively. For Al-terminated (111)/ISG side, shown in Figure 9a, well-arranged [SiO_4] tetrahedron can be observed above the Al layer from crystal, owing to its high polarity. In addition, some B atoms are also segregated from ISG to the surface area. Figure 9b shows the O terminated (111) surface. It can be seen that substantial amount of B atoms along with Al atoms absorbed from ISG forming bonds with O atoms at the outer layer of crystal.

The atomic density profiles of (111)/ISG interface are then showed in Figure 10. Near the Al-terminated side, the density profiles indicate well defined O, Si, and Na layers, which agrees with the crystal-like [SiO_4] tetrahedron in Figure 9a. For the O-terminated side, the profiles show distinct peaks of Al, B, and Zr, which indicates an ordering of these cation segregated from the glass growing on O-terminated side of crystal.

High resolution z-density profiles within about the 10 Å near the interfaces of both sides of (111)/ISG containing species from both crystal and ISG are summarized in Figure 11. The thick solid lines represent the atoms from glass, while the dashed lines are the ones from crystals. It can be seen that at O-terminated side (Figure 11a), the first set of peaks from ISG above the crystal outer layer contains Si, Al and B ions, and overlapping with O atoms segregated from crystal. Interestingly, a hint of B peak is observed at the crystal region, further confirming the ion exchange at the interface area. After the first set, a substantial amount of O atoms are segregated from ISG, forming high intensity peak at about 28.5 Å.

The Al-terminated side has the opposite direction of dipole moment against O-terminated side, which results in different atoms distribution. As shown in Figure 11b, the first peak from the atoms in the glass is the O peak just above the outer Al layer from crystal. The next and third peaks denote to Si and O atoms from ISG, locating about 0.5 and 2Å from the first O peak,

respectively. For one thing, the high sharp peaks of O and Si atoms indicate the corresponding atoms sitting at same *xy* plane. For another, the location of these three peaks are consistent with the ones of O, Si, and O layers marked in Figure 9a, in which the well-defined crystal-like layers construct array of parallel [SiO_4] tetrahedra, with the same position on interface-normal direction.

The outer three peaks of crystal part in Figure 11b denote to O (at around 59.5 Å), Si (at around 60 Å), and O (at around 61.5 Å) layers in Figure 9a, respectively. A [SiO_4] tetrahedron was placed at corresponding z position for demonstration in Figure 11b. The second (Si) and third (O) peaks have a distance of 1.5 Å, which is close to the Si-O bond length, thus corresponding to the Si and O1 atoms, respectively. In addition, the similar heights of these two peaks indicates that the most of corresponding Si and O atoms form the Si-O bonds with similar distances and directions, contributing to the O-Si layers in Figure 9a. While the distance between the first O peak and the second Si peak is about 0.5 Å, matching the positions of O2, O3, O4, and Si from the demonstrated [SiO_4] tetrahedron. Secondary to the distance is that the height of first O peak is about 5 times larger than the second and third peaks, while the ratio between O and Si in [SiO_4] tetrahedron at first and second layers is 3/1, meaning only part of O atoms from the first O layer are bonded with Si atoms.

3.4 Structures of $NiFe_2O_4$(110)/ ISG interfaces

For the $NiFe_2O_4$/ISG interface, the density profiles were also performed to demonstrate segregation and movement of different species. As shown in Figure 12, the atomic density profiles for $NiFe_2O_4$(110)/ISG indicate distinct peaks of Ca, Zr, B, and Al for FeO-terminated side, and Ca, Al, Si, and O for NiFeO-terminated side. Similar to $MgAl_2O_4$/ISG interface, these high sharp peaks near crystal surfaces indicate certain degrees of ordering of these ions segregated from the glass. Despite of the difference of spinel crystal, the Al and O peaks at NiFeO-terminated side are obviously higher than those at NiO-terminated side. This is because the $NiFe_2O_4$ and $MgAl_2O_4$ (110) have similar stacking sequence, …FeO – NiFeO – FeO – NiFeO…. The next layer after NiFeO belongs to FeO layer, which is the reason leading to the segregation of Al from ISG.

The high density profiles include both crystal (dashed lines) and glass (solid lines) within about 10 Å near both sides of $NiFe_2O_4$(110)/ISG interface are plotted, in order to take a close investigation of atom distribution. Near FeO-terminated side, the peak of O species from glass with high intensity along with Si and B peaks were absorbed into the AlO-terminated (110) surface. In addition, Fe and O ions originally from outer layer of crystal are observed near 22 Å, overlapping with the first set of peaks of O, Si, and B from glass. Meanwhile, the B species from glass moved into the outer FeO crystal layer, from which the peak has same heights with those from Fe and O observed in glass. This ion exchange phenomenon was also observed in $MgAl_2O_4$/ISG interface models. Interestingly, although the two sets of interface models contain different crystals, it is always B species from glass that segregate into crystal layers.

For NiFeO-terminated side, shown in Figure 13b, no ion exchange was observed on both crystal and glass regions, which indicates this phenomenon highly depends on the orientation of crystal. In addition, overlapping of high intensity of O and relatively low intensity of B and Al peaks from ISG are observed near the crystal surface, following by the Si peak overlapping with O and B.

3.5 Structures of $NiFe_2O_4$(111)/ISG interfaces

Figure 14 shows the atomic density profiles of ISG for $NiFe_2O_4$(111)/ISG. Similar to $MgAl_2O_4$(111) plane, the $NiFe_2O_4$(111) surface has a layer stacking sequence of anion – cation – anion – cation…, indicating high polarity along surface normal direction. The $NiFe_2O_4$(111) plane used to generate interface contains O-terminated on one side and Fe-terminated on another side. It is found that the intensity of Ca, Na, Si, and O species are clearly higher near Fe-terminated surface, which indicates an ordering of these atoms segregated from the glass. On the other side of $NiFe_2O_4$(111) surface, the O atoms in the outer layer attract most of cations from glass, resulting in the segregation of Ca, Zr, B, and Al to the surface area. In addition, peaks of different species show distinct magnitudes of decay. For Si and B, the peaks closed to crystal surfaces gradually decay into glass bulk. While for O, Na, Zr, and Al, these peaks near crystal surfaces are much higher than the rest of the glass. Compared to $MgAl_2O_4$(111)/ISG interface, the segregated atoms from ISG are quite similar. In addition, the density profiles near metal-terminated side from both $MgAl_2O_4$(111)/ISG and $NiFe_2O_4$(111)/ISG show high sharp O and Si peaks, indicating the crystal-like Si-O layers forming on the cation-terminated crystal surface.

High resolution z-density profiles of O, Si, Al, and B from glass, along with three species from $NiFe_2O_4$(111) crystal within 10 Å of interfaces around both sides of (111) surface are showed in Figure 15. At Fe-terminated side (Figure 15a), the first high first peak from glass denote to O, followed by a short Si peak. The next O peak, though relatively small, locates at around 19.2 Å, occurring at about 1.7 Å from the Si peak. The locations of these three peaks agree well with the O-Si-O layers in the high ordered O-Si-O peaks in caption image in Figure 15a. Similar to $MgAl_2O_4$(111), the three well defined O, Si, and O layers from $NiFe_2O_4$(111) Fe-terminated side construct a row of ordered parallel [SiO_4] tetrahedra, with the same position on interface-normal direction.

For the O-terminated crystal surface side, showed in Figure 15b, the first set of peaks from glass consists of all the glass former, Al, Si, and B, partially overlapping with the outer O layer of $NiFe_2O_4$(111). Due to the accumulation of cations at the crystal surface, the high sharp O peak was formed right after. This anion-cation layers segregated from glass indicate high ordering structure near crystal surface, which highly depends on the surface orientation and results from the crystal growth after melt-quench process.

3.6 Ordering of cations at the glass/crystal interfaces

It has been known from previous z-density profiles that for all the $MgAl_2O_4$/ISG and $NiFe_2O_4$/ISG interfaces, atoms from ISG show different concentrations between interface area and glass bulk area. Therefore, total correlation function and coordination number distribution analysis for three chosen regions for each interface model were then take into investigation; the crystal part, the interface region from ISG, and the bulk region. For interface model, since the ISG part contains finite atoms, the concentration change at the interface region would affect the concentration at bulk region. Therefore, the results from pure ISG were included as a reference. Here only B and Al species were investigated since the coordination number of these two ions highly depends on the concentration of glass. In addition, the coordination number as well as the bond length for B and Al in glass are quite different from those in crystal. However, for Si, the length of Si-O bond showed very similar behavior in both silicate glass and crystalline silica.

Figure 16 and 17 show the total correlation function and coordination number distribution of B-O pair and Al-O pair of $MgAl_2O_4$(110)/ISG and $MgAl_2O_4$(111)/ISG, respectively. The

interface region from ISG is marked in black, including atoms within around 5 Å above the outer layer of crystal. The bulk region from ISG is marked in red, sitting around 20 Å away from crystal surface. The crystal region is marked in yellow, while the curve representing pure ISG is marked in blue. For B-O pair, we can see that the first peak, which represents three-coordinated B, of bulk region from ISG part is highest, followed by interface region and then pure ISG. On the other hand, the sequence of second peaks, which denotes to four-coordinated B, are opposite against the first ones. The pure ISG has the highest concentration of four-coordinated B, while the bulk region of ISG part from interface has the lowest concentration of it. For Al-O pair, shown in Figure 16b and 17b, the bond length is around 1.91 Å in crystal, longer than that in bulk region from ISG and pure ISG. Interestingly, the Al-O pairs from interface part from ISG are more crystal-like since the pair distribution function of these two are almost overlapping with each other. In addition, the coordination number for Al at interface region is very similar to that in crystal. All of these results indicate the ordering and crystal growth near the crystal surface.

Different from $MgAl_2O_4$/ISG interfaces, the Ni and Fe in crystal part of $NiFe_2O_4$/ISG interface cannot be found in ISG part. Therefore, the crystal growth upon $NiFe_2O_4$ surfaces show distinct behaviors on magnitude. Figure 18 and 19 display the total correlation function and coordination number distribution of B-O and Al-O pair of $NiFe_2O_4$(110)/ISG and $NiFe_2O_4$(111)/ISG, respectively. For B-O pair, the highest peak of three-coordinated B comes from bulk region of ISG part in both of (110)/ISG and (111)/ISG interfaces, while the pure ISG shows the lowest height on this peak, which differs from $MgAl_2O_4$/ISG interfaces. Interestingly, the four-coordinated B peak in the interface region in the $NiFe_2O_4$(110)/ISG model show higher intensity than the other two (Figure 18a). But for $NiFe_2O_4$(111)/ISG interface models. The B from interface and bulk region of ISG show similar behavior on total correlation function as well as coordination number (Figure 19a).

As for Al atom in $NiFe_2O_4$(110)/ISG, showed in Figure 18b, the bond length of Al-O in interface region from ISG is slightly longer than that in bulk region and pure ISG, however much shorter compared to that in $MgAl_2O_4$(110)/ISG interface, as well as the coordination number of Al. This result indicates that the Al atoms segregated to the $NiFe_2O_4$(110)/ISG interface are more glass-like in both bond length and coordination number than those near $MgAl_2O_4$(110)/ISG interface. For $NiFe_2O_4$(111)/ISG, showed in Figure 19b, the Al atoms

demonstrate almost same behavior on both bond length and coordination number distribution. Therefore, despite of the segregation of Al to both $MgAl_2O_4$/ISG and $NiFe_2O_4$/ISG, the Al atoms show distinct degree of ordering that highly depend on the crystal part.

4. Discussions

Ordering and preferential distribution near the crystal surfaces were evidenced by the results of density profile analysis of the interface structures of both $MgAl_2O_4$/ISG and $NiFe_2O_4$/ISG interface models, with sharp peaks near the crystal surface representing the species segregated from ISG bulk and indicating an ordered local structure as compared to more random distribution in the bulk glass. In addition, the coordination number change of Al, which shows distinct behaviors on CN and bond length in crystal and glass, gave another direct evidence on the occurring of ordered structure. It can be seen in Figure 16 and 17 that Al atoms have a coordination number of six in crystal and four in the glass bulk. While for Al from glass near interface area, the curves almost overlapped with the ones from crystal, indicating the Al species near both $MgAl_2O_4$(110)/ISG and $MgAl_2O_4$(111)/ISG interfaces are more crystal-like.

As for the B ion, the relative percentages of B^3 and B^4 are highly depended on the glass compositions, which can be observed in Figure 16a-19a. It can be seen that the TDF curve for B ion contains two peaks, which denotes to three coordinated- and four coordinated-B, respectively. For all the four interface structures, the three-coordinated-B peak locates at around 1.46 Å for B from glass bulk area, and it shifts to around 1.47 Å for B from ISG, along with the intensity decreases. While the peak of 4-coordinated B from glass bulk is higher than that from ISG. For B from interface area, the positions and heights of peaks for $MgAl_2O_4$(110)/ISG, $MgAl_2O_4$(111)/ISG, and $NiFe_2O_4$(110)/ISG interface models are between glass bulk area and ISG, while the peak of B from interface area almost overlaps with that from glass bulk area for $NiFe_2O_4$(111)/ISG interface model.

Distribution of Al and B coordination species for pure ISG and the four interfaces are summarized in Table 5 and 6, respectively. For Al species, 99.3% of them have a coordination number of 4 in pure ISG and 0.7% of them are three-coordinated, while no five-fold Al is observed. This indicates that Al acts as glass former in ISG. However, ISG show distinct behaviors of coordination number when forming interface. It can be seen in Table 5 that for all of the spinel/ISG interface models, the amount of four-coordinated Al is less than that in pure ISG.

In addition, the five coordinated Al ions appear at all the four interface models, which cannot be found in pure ISG. The increase of Al coordination number is caused by inadequate glass modifiers to compensate the extra negative charge of $[AlO_4]$ [30,39]. In this case, the local composition changes in ISG when forming interface with spinel $MgAl_2O_4$ and $NiFe_2O_4$ is the reason of the existence of high-coordinated Al in the glass part of spinel/ISG interface.

For five-coordinated Al, the $MgAl_2O_4$ and $NiFe_2O_4$ spinel(110)/ISG models have concentration of 2.6% and 2.20%, respectively, higher than the $MgAl_2O_4$ and $NiFe_2O_4$ (111)/ISG models, which have concentrations of 0.7% and 0.73%, respectively. Similar results of concentration changes of Al in α-Al_2O_3/Calcium–Alumino–Silicate glass were reported by Zhang and Garofalini[20].

The percentage of Boron species of pure ISG, $MgAl_2O_4$(110)/ISG, $MgAl_2O_4$(111)/ISG, $NiFe_2O_4$(110)/ISG, and $NiFe_2O_4$(111)/ISG interface models are summarized in Table 6. It can be shown that the concentration of B^3 in pure ISG is lower than that in spinel/ISG interface models, whereas the B^4 concentration is higher. When forming interface with spinel crystals, the ISG have different B^3 and B^4 values, demonstrated in Table 6. The B^4 concentration of all the four interface models are lower than that of pure ISG. For $MgAl_2O_4$/ISG, the (110)/ISG has the B^4 value of 48.87%, higher than (111)/ISG. Interestingly, the trend is similar in $NiFe_2O_4$/ISG interfaces, in which the (110)/ISG has higher B^4 value. The coordination of Boron is highly composition depended due to two reasons. Firstly, the formation of interfaces cause redistribution of glass formers in ISG part, resulting in conversion between B^3 and B^4. Secondly, the local composition change affect the coordination number change as a function of composition by using this set of potentials[10].

Density profile analysis of the interface structures generated from MD simulation method indicate crystallization occurring near the crystal surface. Higher peak intensity results in higher ordered local environments. Usually, it is difficult to observe the long range order structure directly. However, for $MgAl_2O_4$ and $NiFe_2O_4$ spinel crystals included interface models, both the Al-terminated (111)/ISG and Fe-terminated (111)/ISG show well-arranged $[SiO_4]$ tetrahedron above the Al and Fe layer of $MgAl_2O_4$ $NiFe_2O_4$ crystals, respectively, which cannot be observed on the other side of this interface structure with O termination on the surface slabs.

To further study this phenomenon, another interface structure with Mg-terminated (111) on one side and O-terminated (111) on the other side was constructed and undergo same melt-quench procedure. Figure 20 shows the snapshots of interface area of Mg- and Al-(111)/glass structures. On the contrary of well-arranged [SiO_4] tetrahedron on the Al-terminated side, the O and Si atoms, though still accumulating near crystal surface, are relatively more disorganized. The reason could be the high dipole moment on Al-terminated (111) surface.

5. Conclusions

The structures of international simple glass (ISG) and its interfaces with low energy surfaces of $MgAl_2O_4$ and $NiFe_2O_4$ spinel structures were investigated by using MD simulations with partial charge pairwise potentials with recent developed boron parameters. Pair distribution functions, bond angle distributions, and *z*-density profile were used to characterize the interfacial structures. The results indicate there exist atomic level ordering of ions on the glass side near glass/crystal interfaces.

The influence of the crystal surface structure on the atom distributions and ordering on the melt/glass side was observed in several different types of interfaces. For the $MgAl_2O_4$(110)/ISG interface, it was found that there exist accumulation of O, Si, and B toward AlO-terminated side and O, Al, B toward MgAlO-terminated side. For the $MgAl_2O_4$(111)/ISG interface, preferential segregation of O, Si, and Na species from ISG bulk onto Al-terminated spinel surface was observed, while Al, B, and Zr segregation was observed near O-terminated side. For $NiFe_2O_4$/ISG, similar trends occurred in the simulations. For the (111) surfaces of both types of spinel crystals, well-arranged [SiO_4] tetrahedron was observed near Al/Fe-terminated sides, which shows indication of initial crystalline growth. In addition, ion exchange between B from ISG and Fe from $NiFe_2O_4$(110) surface was observed from simulations, possible due to similar charge and ionic sizes.

The ordering on the glass side show indication of initial stage of crystal growth. According to total correlation function analysis of selected interface area, higher-coordinated Al and Fe species (both are four in the glass, but six in crystals) were founded on the glass side of the interface regions, indicating the initial stage of formation of crystal-like structures. In addition, the distribution of B^3 and B^4 varies noticeably in ISG bulk and that of the interface

region, highlighting the influence of crystal surface structure on that of the adjacent glass regions.

6. Acknowledgement

This research is being performed using funding received from the DOE Offices of Nuclear Energy and Environmental Management through the Nuclear Energy University Programs under Grant No. DE-NE0008597.

References

1. Pegg IL. Turning nuclear waste into glass. *Phys Today* 2015; 68: 33–39.

2. Collin M, Fournier M, Frugier P, et al. Structure of International Simple Glass and properties of passivating layer formed in circumneutral pH conditions. 2018; 2 (1): 2397-2106

3. Ojovan MI, Lee WE. Chapter 17 - Immobilisation of Radioactive Wastes in Glass. In: Ojovan MI, Lee WE (eds) *An Introduction to Nuclear Waste Immobilisation*. Incollection, Oxford: Elsevier, 2005, pp. 213–249.

4. Rushton MJD, Grimes RW, Owens SL. Partial ordering of glass networks adjacent to simulated glass–crystal interfaces. *J Non Cryst Solids* 2011; 357: 3278–3287.

5. Deshkar A, Ahmadzadeh M, Scrimshire A, et al. Crystallization behavior of iron- and boron-containing nepheline ($Na_2O \cdot Al_2O_3 \cdot 2SiO_2$) based model high-level nuclear waste glasses. *J Am Ceram Soc* 2018; 4: 1–21.

6. Shaharyar Y, Cheng JY, Han E, et al. Elucidating the Effect of Iron Speciation (Fe^{2+}/Fe^{3+}) on Crystallization Kinetics of Sodium Aluminosilicate Glasses. *J Am Ceram Soc*; 99: 2306–2315.

7. Mauro JC, Philip CS, Vaughn DJ, et al. Glass Science in the United States: Current Status and Future Directions. *Int J Appl Glas Sci*; 5: 2–15.

8. Gin S, Abdelouas A, Criscenti LJ, et al. An international initiative on long-term behavior of high-level nuclear waste glass. *Mater Today* 2013; 16: 243–248.

9. Du J. *Challenges in Molecular Dynamics Simulations of Multicomponent Oxide Glasses*. Springer International Publishing, 2015.

10. Wu J, Stebbins JF. Effects of cation field strength on the structure of aluminoborosilicate glasses: High-resolution ^{11}B, ^{27}Al and ^{23}Na MAS NMR. *J Non Cryst Solids* 2009; 355: 556–562.

11. Smedskjaer MM, Mauro JC, Youngman RE, et al. Topological principles of borosilicate glass chemistry. *J Phys Chem B* 2011; 115: 12930–12946.

12. Du LS, Stebbins JF. Network connectivity in aluminoborosilicate glasses: A high-resolution ^{11}B, ^{27}Al and ^{17}O NMR study. *J Non Cryst Solids* 2005; 351: 3508–3520.

13. Smedskjaer MM, Youngman RE, Mauro JC. Principles of Pyrex® of glass chemistry: structure - property relationships. *Appl Phys A* 2014; 116: 491–504.

14. Cormier L, Galoisy L, Delaye JM, et al. Short- and medium-range structural order around cations in glasses: amultidisciplinary approach. *Comptes Rendus l'Academie des Sci Ser IV Phys* 2001; 2: 249–262.

15. Barlet M, Kerrache A, Delaye JM, et al. SiO_2-Na_2O-B_2O_3 density: A comparison of experiments, simulations, and theory. *J Non Cryst Solids* 2013; 382: 32–44.

16. Delaye JM. Modeling of multicomponent glasses: a review. *Curr Opin Solid State Mater Sci* 2001; 5: 451–454.

17. Kieu LH, Delaye JM, Cormier L, et al. Development of empirical potentials for sodium borosilicate glass systems. *J Non Cryst Solids* 2011; 357: 3313–3321.

18. Blonski S, Garofalini SH. Molecular Dynamics Study of Silica−Alumina Interfaces. *J Phys Chem* 1996; 100: 2201–2205.

19. Blonski S, Garofalini SH. Atomistic Structure of Calcium Silicate Intergranular Films in Alumina Studied by Molecular Dynamics Simulations. *J Am Ceram Soc* 1997; 80: 1997–

2004.

20. Zhang S, Garofalini SH. Molecular Dynamics Computer Simulations of the Interface Structure of Calcium–Alumino–Silicate Intergranular Films between Combined Basal and Prism Planes of α-Al_2O_3. *J Am Ceram Soc* 2005; 88: 202–209.

21. Litton DA, Garofalini SH. Atomistic Structure of Sodium and Calcium Silicate Intergranular Films in Alumina. *J Mater Res* 1999; 14: 1418–1429.

22. Jiang Y, Garofalini SH. Role of Lu and La in the intergranular films on growth of the prism surface in β-Si_3N_4: A molecular dynamics study. *Scr Mater* 2016; 113: 97–100.

23. Sun W, Du J. Local ordering and interfacial structure between spinel crystal and aluminosilicate glasses from molecular dynamics simulations. *Int J Appl Glas Sci* 2019; 10**:** 41-56.

24. Deng L, Du J. Development of effective empirical potentials for molecular dynamics simulations of the structures and properties of boroaluminosilicate glasses. *J Non Cryst Solids* 2016; 453: 177–194.

25. Gale JD. GULP: A computer program for the symmetry-adapted simulation of solids. *J Chem Soc Faraday Trans* 1997; 93: 629–637.

26. Deng L, Du J. Development of boron oxide potentials for computer simulations of multicomponent oxide glasses. *J Am Ceram Soc*; DOI: 10.1111/jace.16082.

27. Du J, Cormack AN. Molecular Dynamics Simulation of the Structure and Hydroxylation of Silica Glass Surfaces. *J Am Ceram Soc* 2005; 88: 2532–2539.

28. Jamal M, Asadabadi SJ, Ahmad I, et al. Elastic constants of cubic crystals. *Comput Mater Sci* 2014; 95: 592–599.

29. Hill R. The Elastic Behaviour of a Crystalline Aggregate. *Proc Phys Soc Sect A* 1952; 65: 349.

30. Xiang Y, Du J, Smedskjaer MM, et al. Structure and properties of sodium aluminosilicate glasses from molecular dynamics simulations. *J Chem Phys* 2013; 139: 44507.

31. Ren M, Du J. Structural Origin of the Thermal and Diffusion Behaviors of Lithium Aluminosilicate Crystal Polymorphs and Glasses. *J Am Ceram Soc* 2016; 99: 2823–2833.

32. Du J. Molecular Dynamics Simulations of the Structure and Properties of Low Silica Yttrium Aluminosilicate Glasses. *J Am Ceram Soc* 2009; 92: 87–95.

33. Zirl DM, Garofalini SH. Structure of Sodium Aluminosilicate Glasses. *J Am Ceram Soc*; 73: 2848–2856.

34. Greaves GN, Fontaine A, Lagarde P, et al. Local structure of silicate glasses. *Nature* 1981; 293: 611.

35. McKeown DA, Waychunas GA, Brown GE. EXAFS study of the coordination environment of aluminum in a series of silica-rich glasses and selected minerals within the Na_2O-Al_2O_3-SiO_2 system. *J Non Cryst Solids* 1985; 74: 349–371.

36. W. Burnham C, J. Buerger M. Refinement of the Crystal Structure of Andalusite. *Zeitschrift Fur Krist - Z Krist* 1961; 115: 269–290.

37. Du J, Cormack AN. The medium range structure of sodium silicate glasses: a molecular dynamics simulation. *J Non Cryst Solids* 2004; 349: 66–79.

38. Lu X, Deng L, Kerisit S, et al. Structural role of ZrO_2 and its impact on properties of boroaluminosilicate nuclear waste glasses. *npj Mater Degrad* 2018; 2: 19.

39. Moore H, McMillan PW. A study of glasses consisting of the oxides of elements of low atomic weight. *J Soc Glas Technol* 1956; 40: 66–96.

40. Sickafus KE, Wills JM, Grimes NW. Structure of Spinel. *J Am Ceram Soc* 1999; 82: 3279–3292.

41. Bruschini E, Speziale S, Andreozzi GB, et al. The elasticity of $MgAl_2O_4$-$MnAl_2O_4$ spinels by Brillouin scattering and an empirical approach for bulk modulus prediction. *Am Mineral* 2015; 100: 644–651.

42. Manassidis I, Gillan MJ. Structure and Energetics of Alumina Surfaces Calculated from First Principles. *J Am Ceram Soc* 1994; 77: 335–338.

43. Fritsch D, Ederer C. Epitaxial strain effects in the spinel ferrites $CoFe_2O_4$ and $NiFe_2O_4$ from first principles. Epub ahead of print 2010. DOI: 10.1103/PhysRevB.82.104117.

44. Li Z, Fisher ES, Liu JZ, et al. Single-crystal elastic constants of Co-Al and Co-Fe spinels. *J Mater Sci* 1991; 26: 2621–2624.

Tables

Table 1: Atomic charges and Buckingham potential parameters [7,27,26]

Pairs	A_{ij} (eV)	ρ_{ij} (Å)	C_{ij} (eV.Å^6)	B_{ij} (eV.Å^6)	D_{ij}	n
$O^{-1.2}$-$O^{-1.2}$	2029.2204	0.343645	192.58	46.462	-0.32605	3.430
$Si^{2.4}$-$O^{-1.2}$	13702.905	0.193817	54.681	28.942	-3.0250	3.949
$B^{1.8}$-$O^{-1.2}$	14877.069	0.171281	28.5	18.980	-4.1189	3.960
$Al^{1.8}$-$O^{-1.2}$	12201.417	0.195628	31.997	51.605	-10.073	3.193
$Na^{0.6}$-$O^{-1.2}$	4383.7555	0.243838	30.70	48.251	-4.7037	2.898
$Mg^{1.2}$-$O^{-1.2}$	7063.4907	0.210901	19.210	54.028	-11.609	2.845
$Ni^{1.2}$-$O^{-1.2}$	12987.7832	0.203164	35.994	73.158	-14.550	3.024
$Fe^{1.8}$-$O^{-1.2}$	11777.0703	0.207132	21.642	104.203	-32.110	2.670

Table 2 Calculation of $MgAl_2O_4$ spinel crystal structure and properties as compared to DFT and experimental values

	This work Potential	Literature	
		EXP[40,41]	DFT [42,23]
V (Å^3)	529.7	528.6	544.5

a (Å)	8.09	8.08	8.16
C11	278.6	283.6	330.8
C12	172.7	156.9	166.2
C44	126.7	154.6	165.3
B (GPa)	208.0	196	221.1
G (GPa)	97.2	108.1	124.9
E (GPa)	164.4	274.6	315.5

Table 3 Calculation of $NiFe_2O_4$ spinel crystal structure and properties as compared to DFT and experimental values

	This work Potential	Literature	
		EXP[43,44]	DFT[43]
V ($Å^3$)	585.1	609.8	600.2
a (Å)	8.3	8.5	8.43
C_{11}	249.2	273.1	252.2

C_{12}	148.5	160.7	139.5
C_{44}	106.0	82.3	93.2
B (GPa)	182.1	198.2	177.1
G (GPa)	73.5	70.6	73.8
E (GPa)	138.2	189.4	194.4

Table 4. Composition of International Simplified Glass (ISG) (*mol %*) (density *2.49g/cm3*)

	SiO_2	B_2O_3	Na_2O	Al_2O_3	CaO	ZrO_2
Mol%	60.1	16.0	12.7	3.8	5.7	1.7

Table 5. Percentage of Al species of pure ISG, $MgAl_2O_4$(110)/ISG, $MgAl_2O_4$(111)/ISG, $NiFe_2O_4$(110)/ISG, and $NiFe_2O_4$(111)/ISG interface models.

	3-CN Al	4-CN Al	5-CN Al
ISG	0.37%	99.63%	
$MgAl_2O_4$(110)/ISG	0.7%	96.7%	2.6%
$MgAl_2O_4$(111)/ISG	0.4%	98.9%	0.7%
$NiFe_2O_4$(110)/ISG	0.73%	97.07%	2.20%
$NiFe_2O_4$(111)/ISG		99.27%	0.73%

Table 6. Percentage of B species of pure ISG, $MgAl_2O_4$(110)/ISG, $MgAl_2O_4$(111)/ISG, $NiFe_2O_4$(110)/ISG, and $NiFe_2O_4$(111)/ISG interface models.

	3-CN B	4-CN B
ISG	45.83%	54.17%
$MgAl_2O_4$(110)/ISG	51.13%	48.87%
$MgAl_2O_4$(111)/ISG	53.91%	46.09%
$NiFe_2O_4$(110)/ISG	52.43%	47.57%
$NiFe_2O_4$(111)/ISG	56.00%	44.00%

Figure captions

Figure 1. Schematic structure of spinel AB_2O_4 structures; ***a*** and ***b***, as-cleaved (100) and (110) models: ***c***, original and redefined (111) model. AB_2O_4 surface. Yellow and blue: metal ions; Red: oxygen ions

Figure 2. schematic structure of initial generated $MgAl_2O_4$(110)/Glass interface model

Figure 3. Schematic showing how systems were quenched to produce interfaces.

Figure 4. Simulated total correlation distribution function for the ISG

Figure 5. Bond angle distributions of the ISG

Figure 6. Schematic structure of ***a***, MgAlO terminated and ***b***, AlO-terminated $MgAl_2O_4$ (110)/ISG. The color of atoms are consistent with the z-density profiles

Figure 7. z-density atomic density profiles of $MgAl_2O_4$(110)/ISG

Figure 8. Higher resolution z-density profiles of O, Al, and Mg atoms in $MgAl_2O_4$(110)/ISG interface.

Figure 9. Schematic structure of Al- and O-terminated $MgAl_2O_4$(111)/ISG. The color of atoms are consistent with the z-density profiles

Figure 10. z-density atomic density profiles of $MgAl_2O_4$(111)/ISG

Figure 11. Higher resolution z-density profiles of atoms in $MgAl_2O_4$(111)/ISG interface.

Figure 12. z-density atomic density profiles in $NiFe_2O_4$(110)/ISG interface.

Figure 13. Higher resolution z-density profiles of atoms in $NiFe_2O_4$(110)/ISG interface.

Figure 14. z-density atomic density profiles in $NiFe_2O_4$(111)/ISG interface.

Figure 15. Higher resolution z-density profiles of atoms in $NiFe_2O_4$(111)/ISG interface.

Figure 16. Total correlation function and coordination number of a, B-O pair, and b, Al-O pair for $MgAl_2O_4$(110)/ISG

Figure 17. Total correlation function and coordination number of a, B-O pair, and b, Al-O pair for $MgAl_2O_4$(111)/ISG

Figure 18. Total correlation function and coordination number of a, B-O pair, and b, Al-O pair for $NiFe_2O_4$(110)/ISG

Figure 19. Total correlation function and coordination number of a, B-O pair, and b, Al-O pair for $NiFe_2O_4$(111)/ISG

Figure 20. Schematic structures of Mg- and Al-terminated (111)/ISG glass interface. The color of atoms are consistent with the z-density profiles

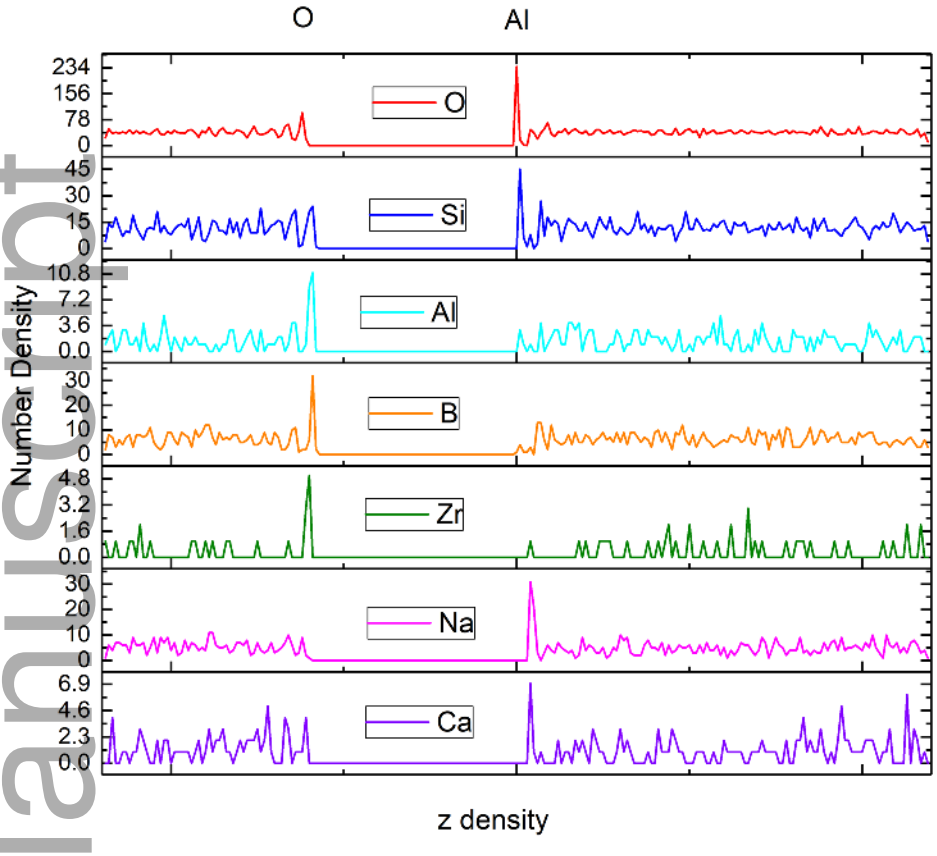

jace_16374_f10.tif

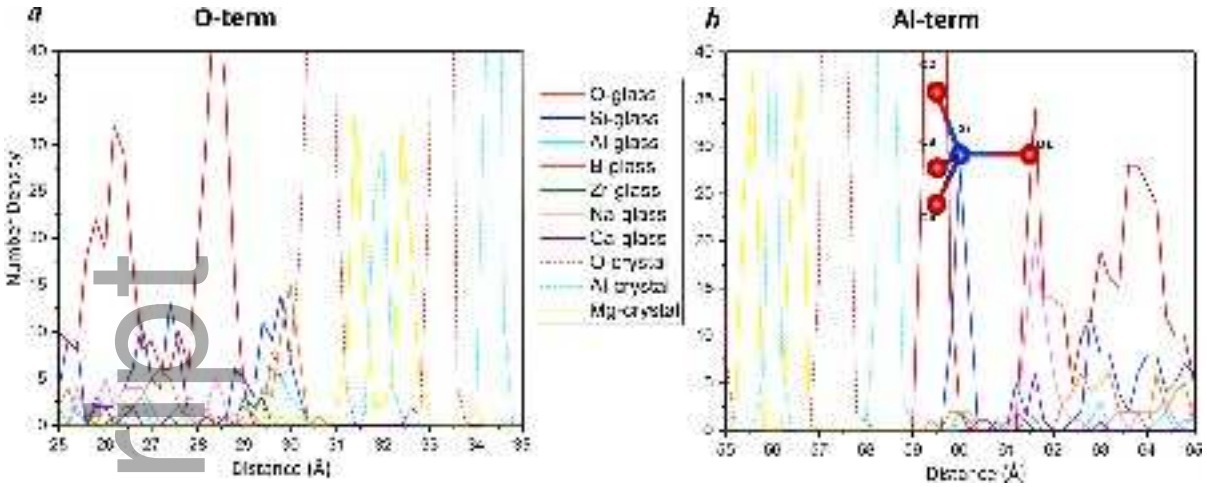

jace_16374_f11.tif

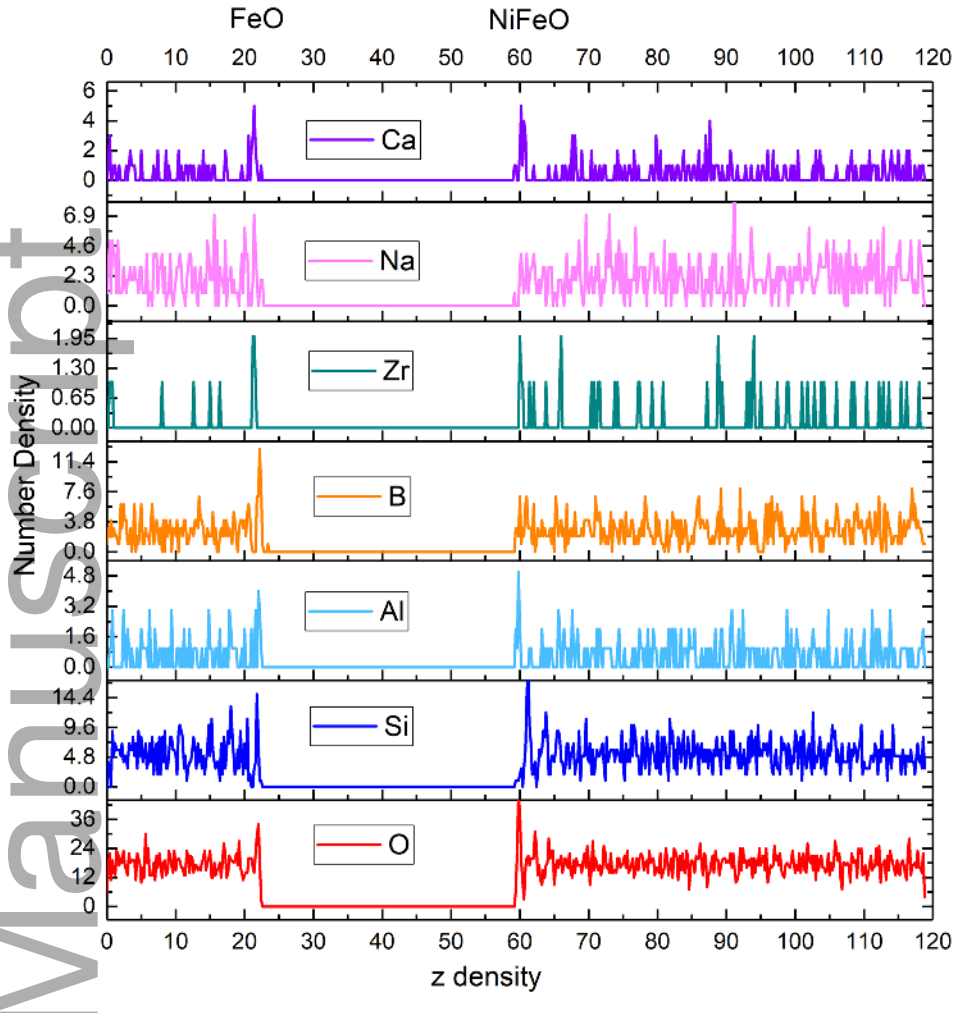

jace_16374_f12.tif

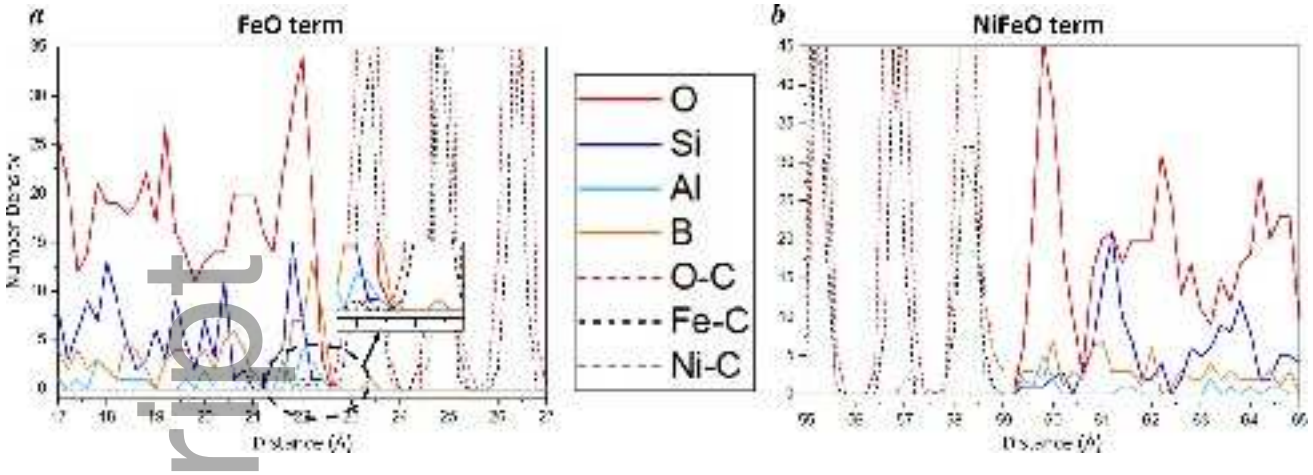

jace_16374_f13.tif

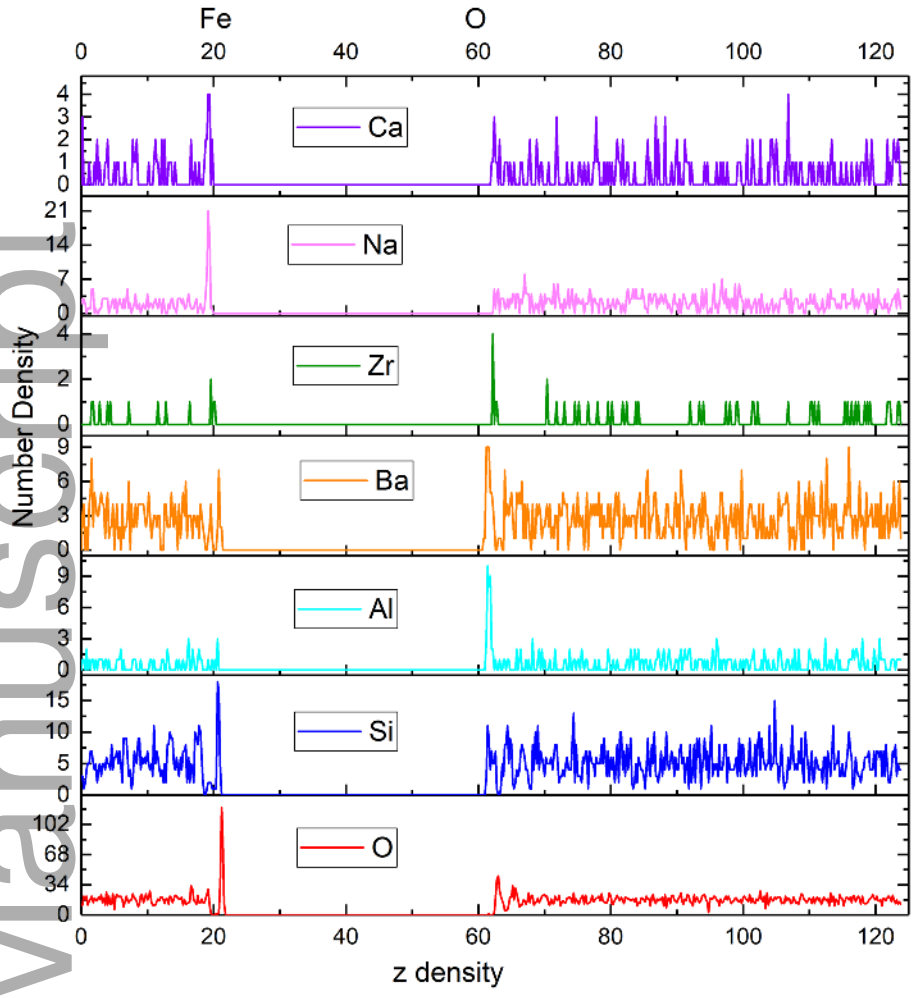

jace_16374_f14.tif

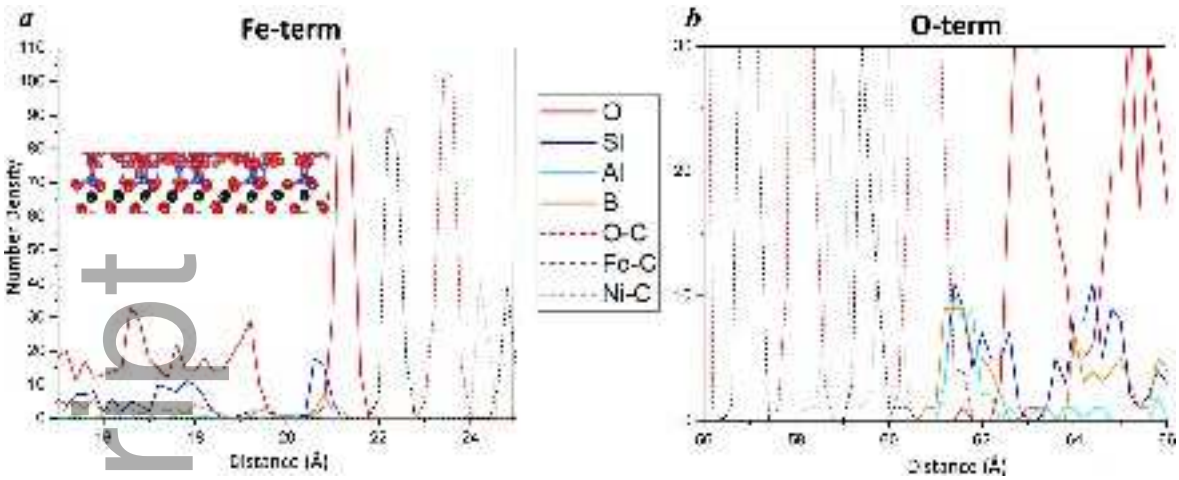

jace_16374_f15.tif

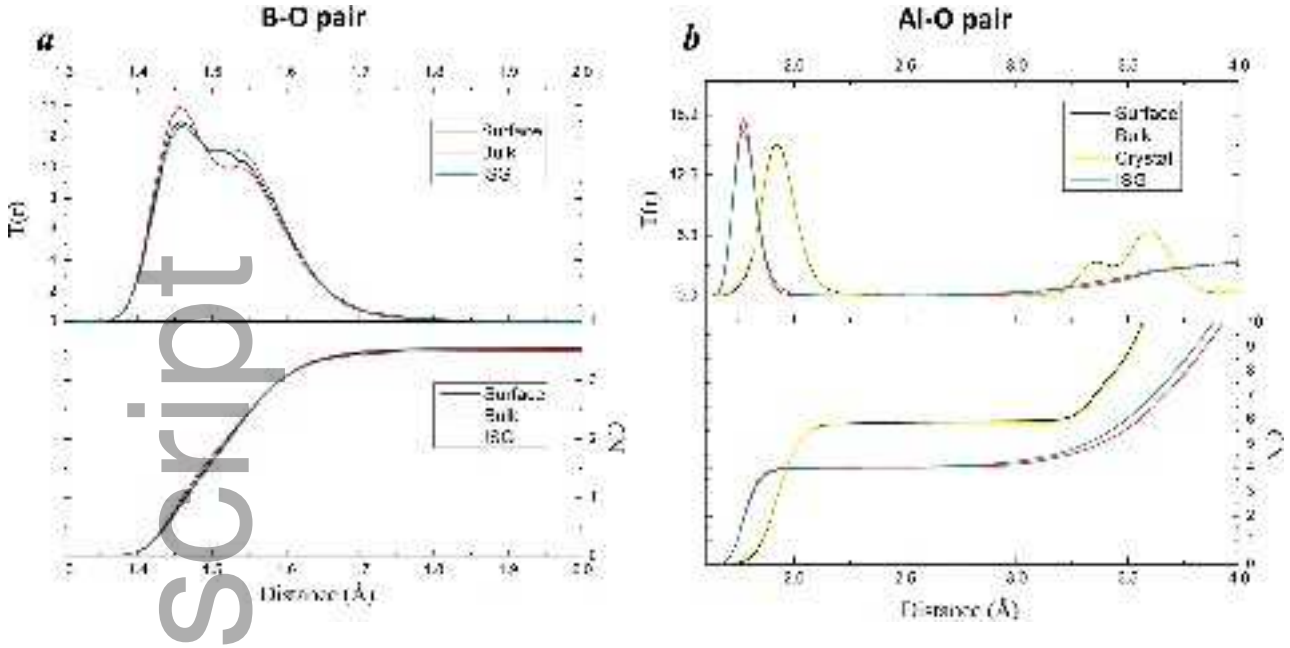

jace_16374_f16.tif

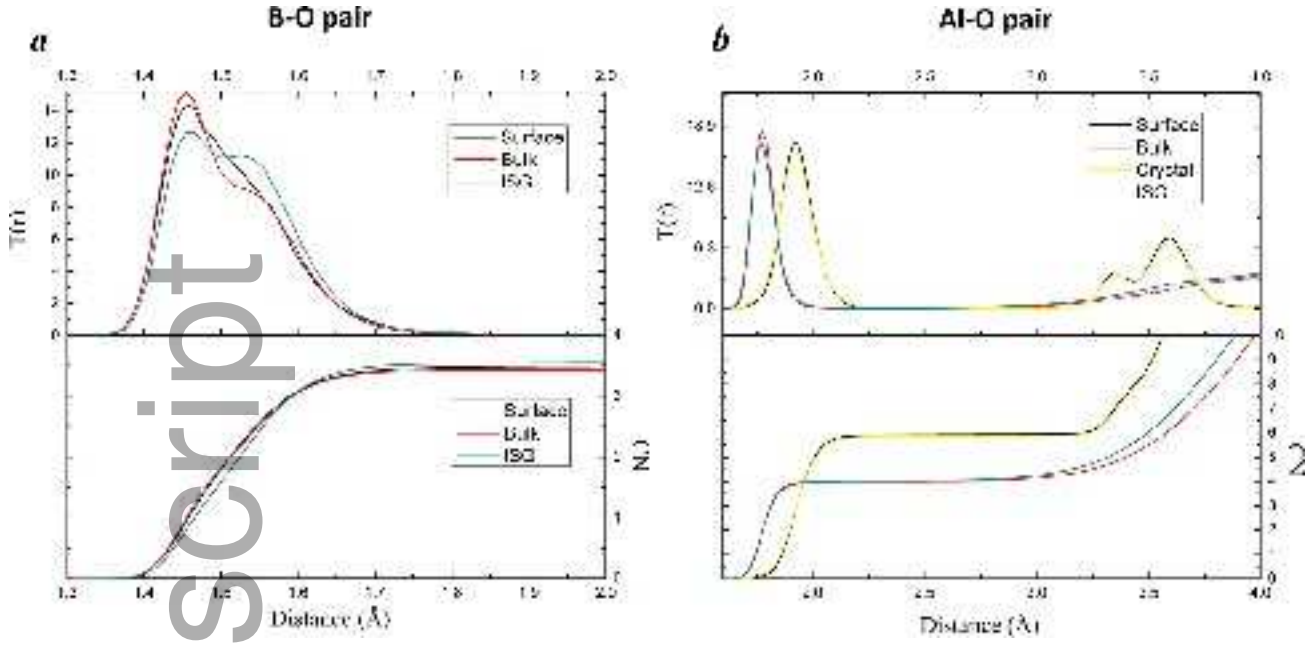

jace_16374_f17.tif

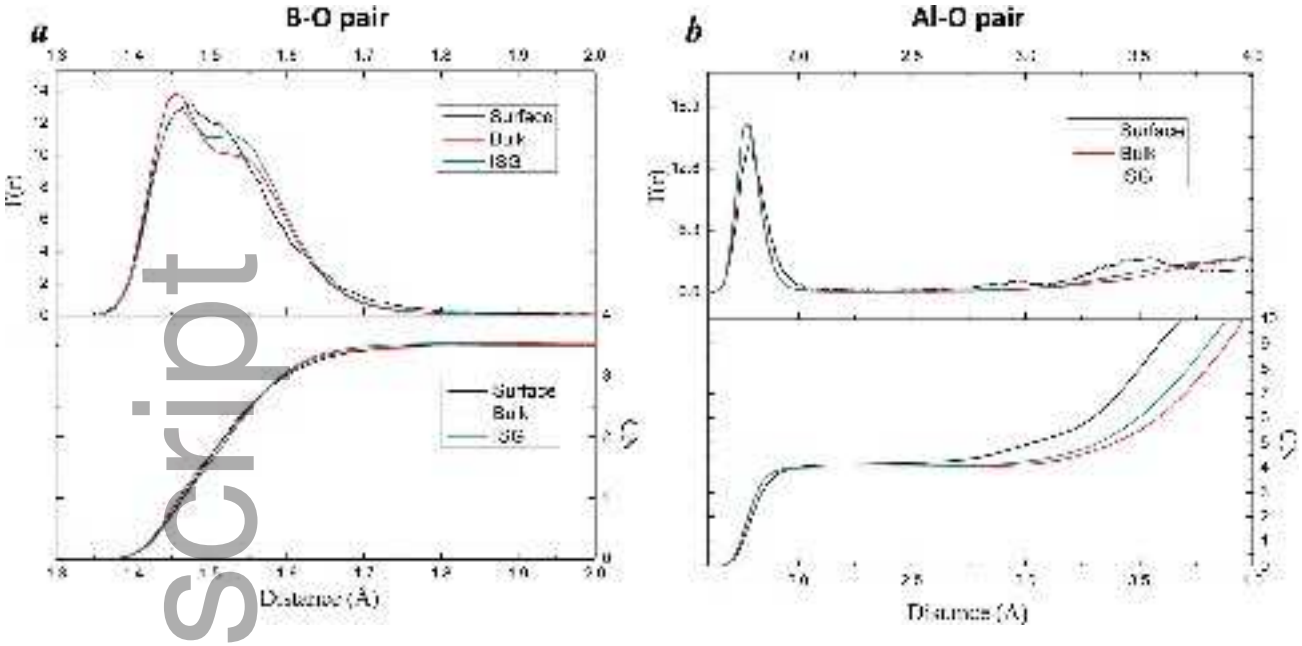

jace_16374_f18.tif

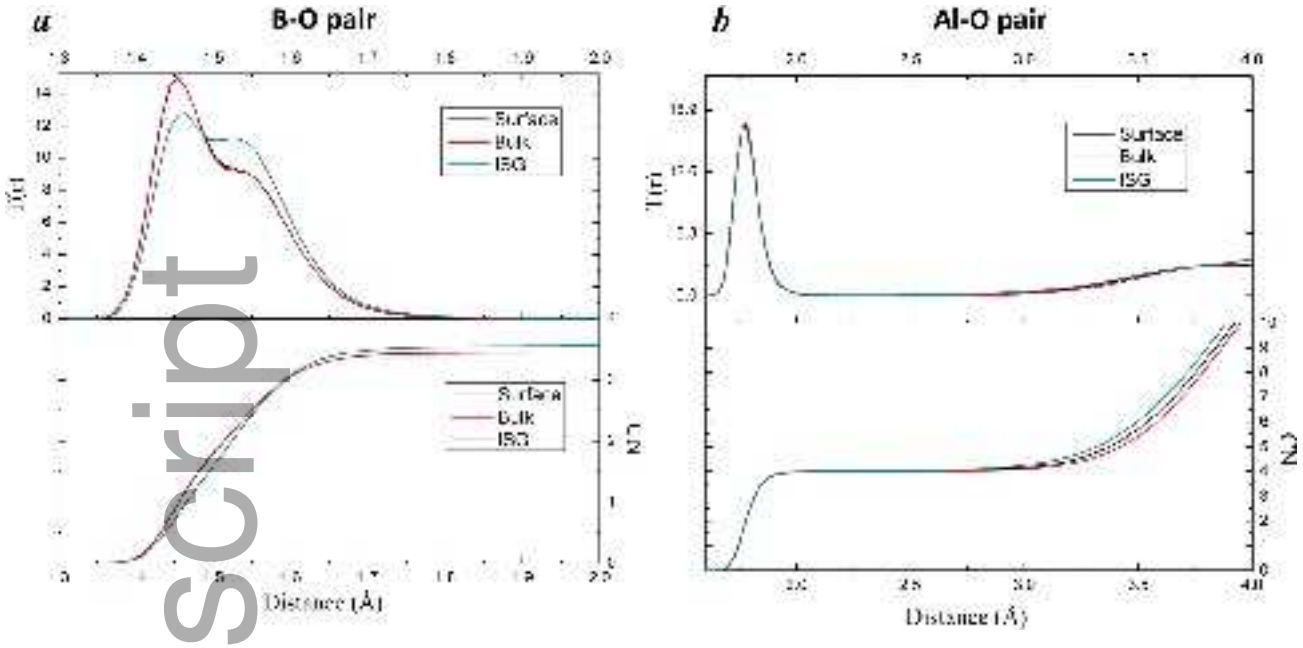

jace_16374_f19.tif

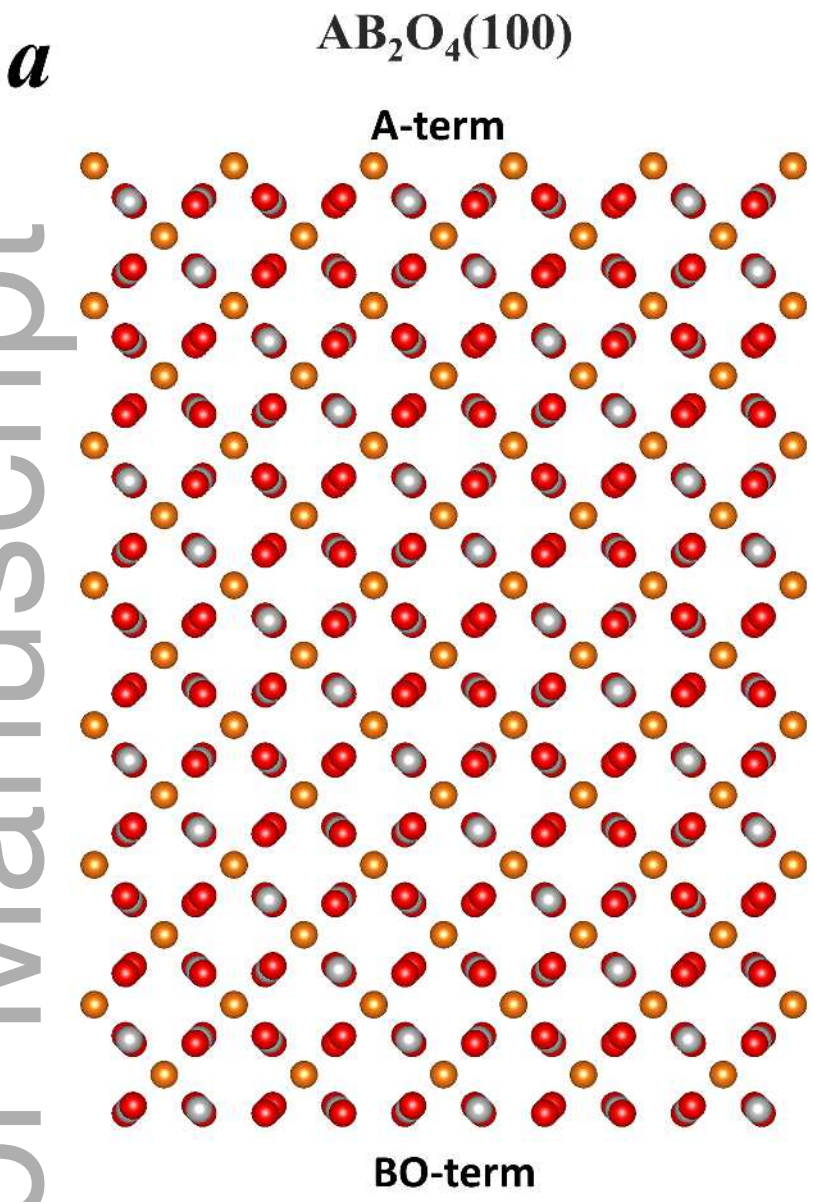

jace_16374_f1a.tif

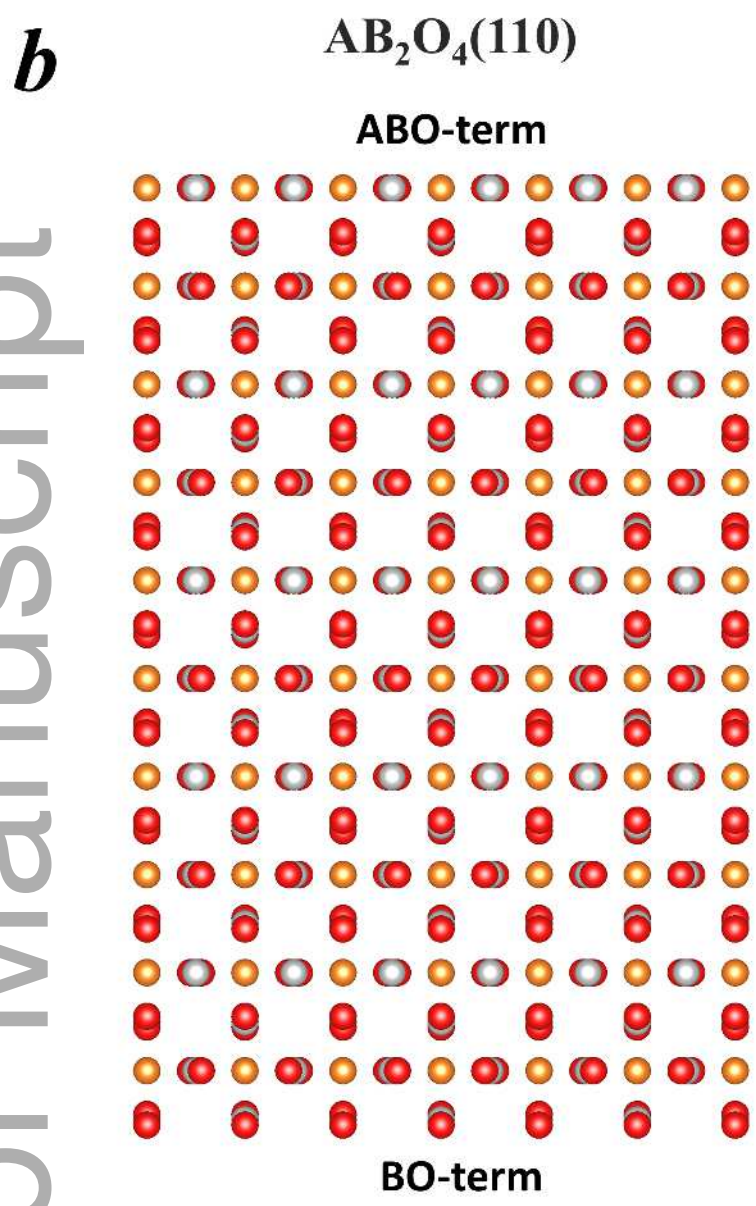

jace_16374_f1b.tif

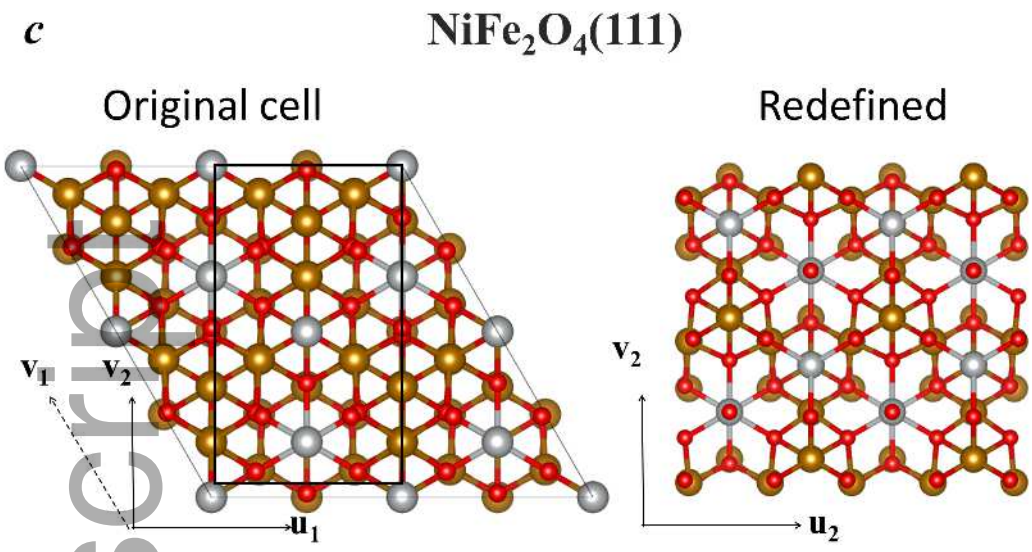

jace_16374_f1c.tif

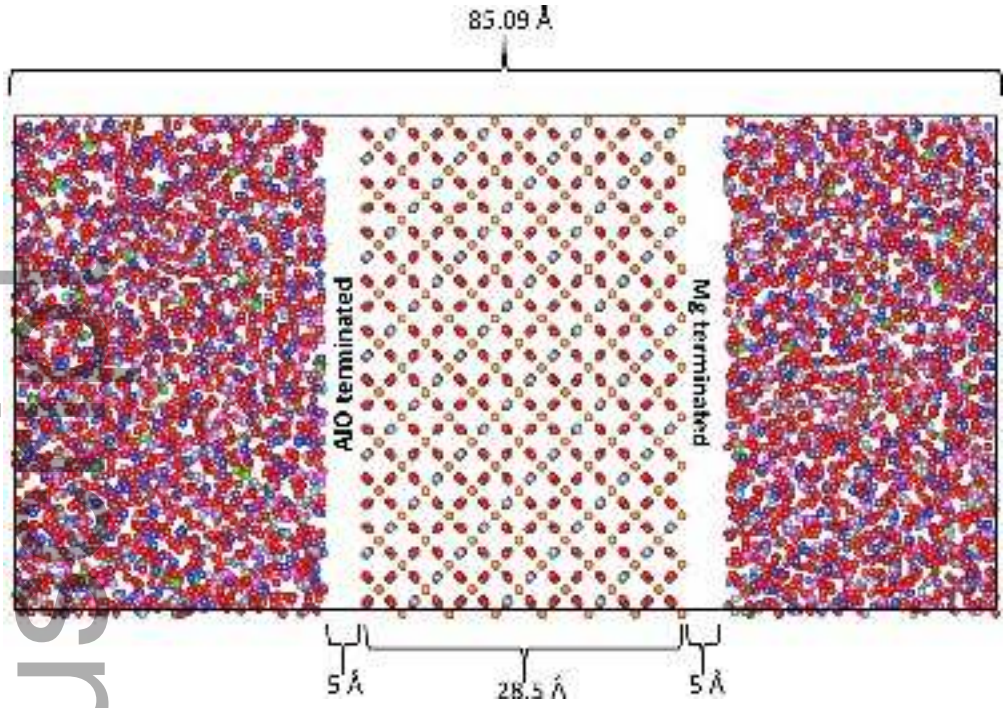

jace_16374_f2.tif

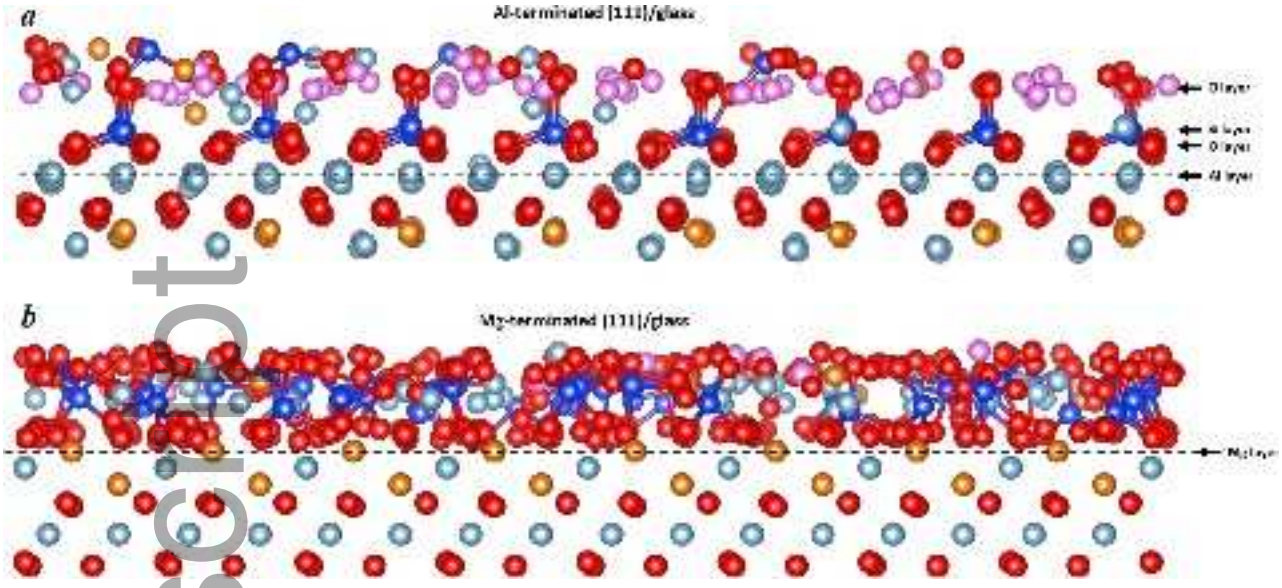

jace_16374_f20.tif

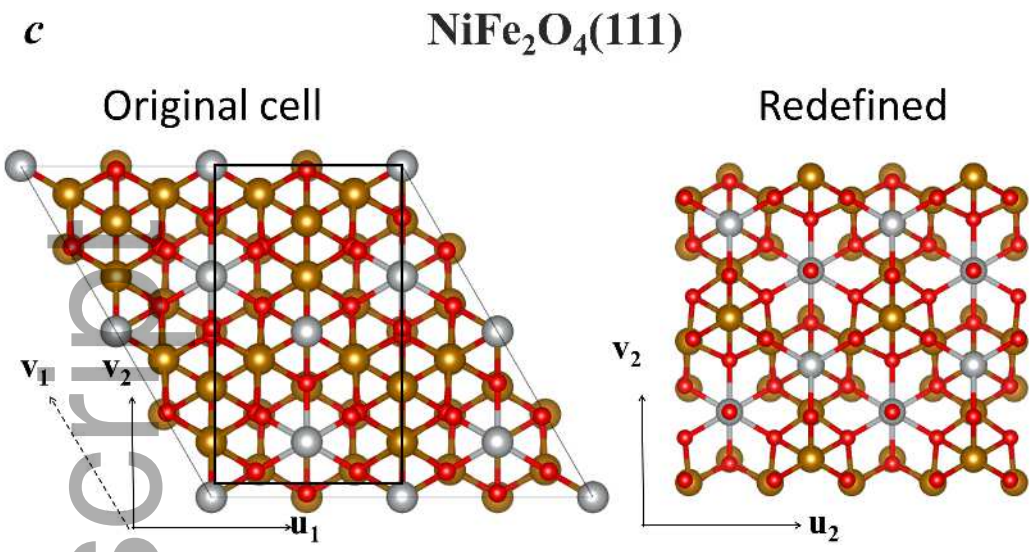

jace_16374_f3.tif

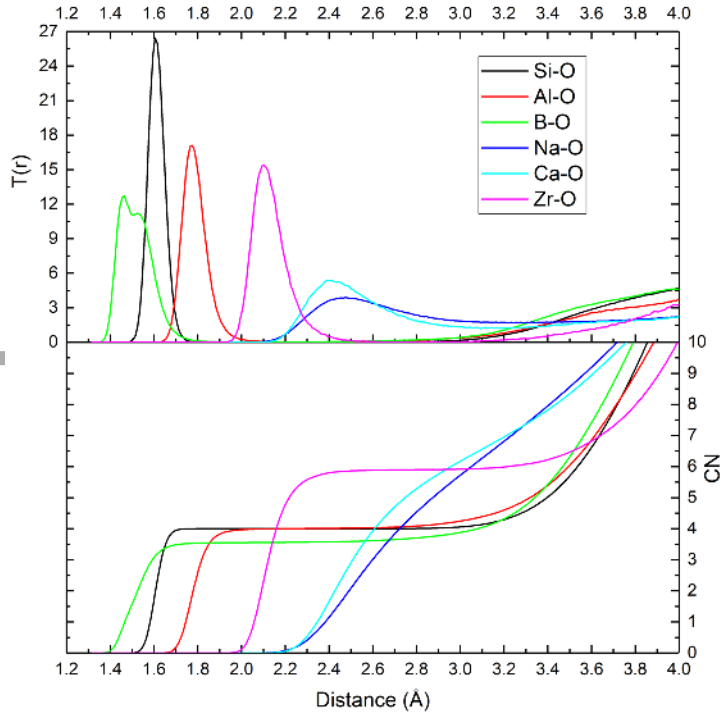

jace_16374_f4.tif

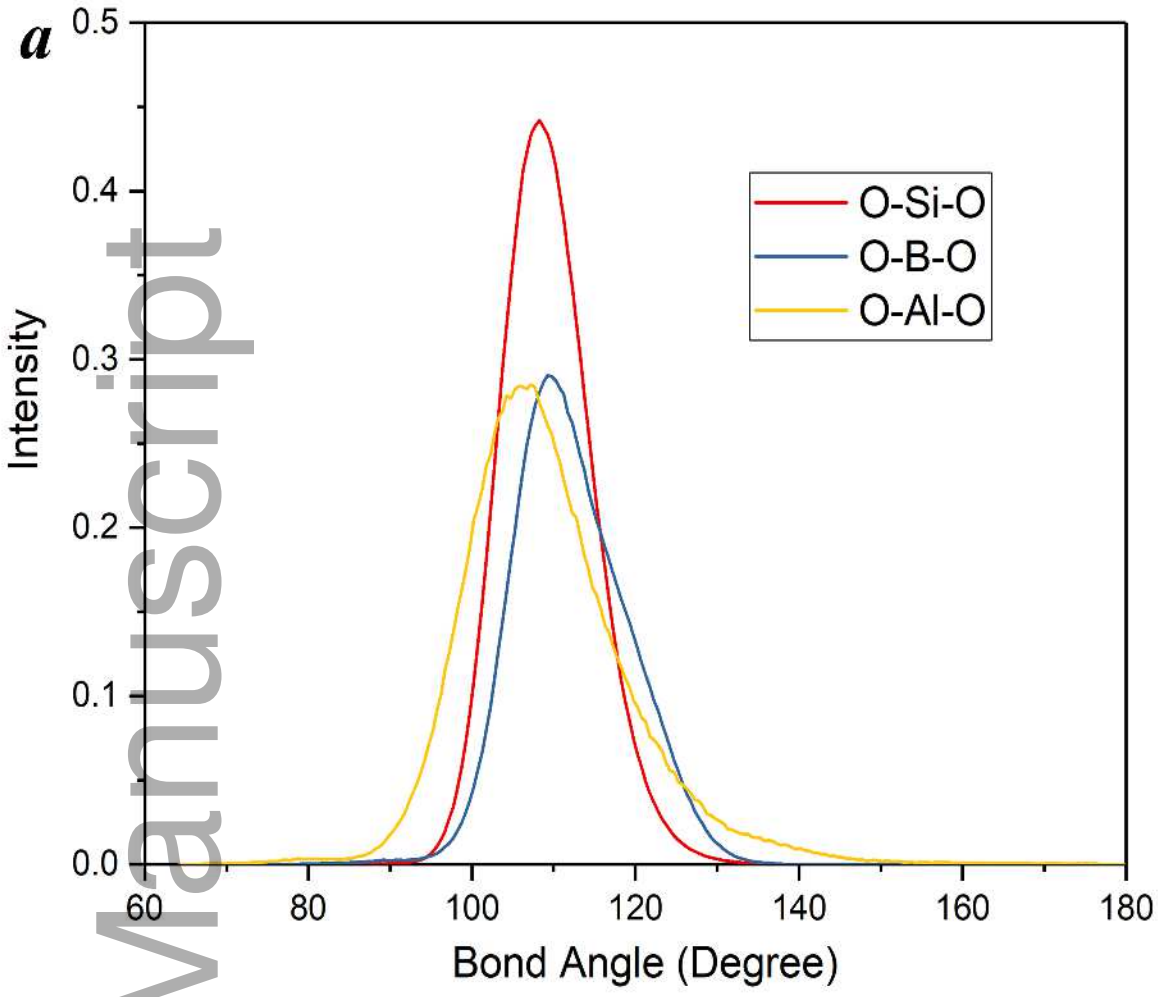

jace_16374_f5a.tif

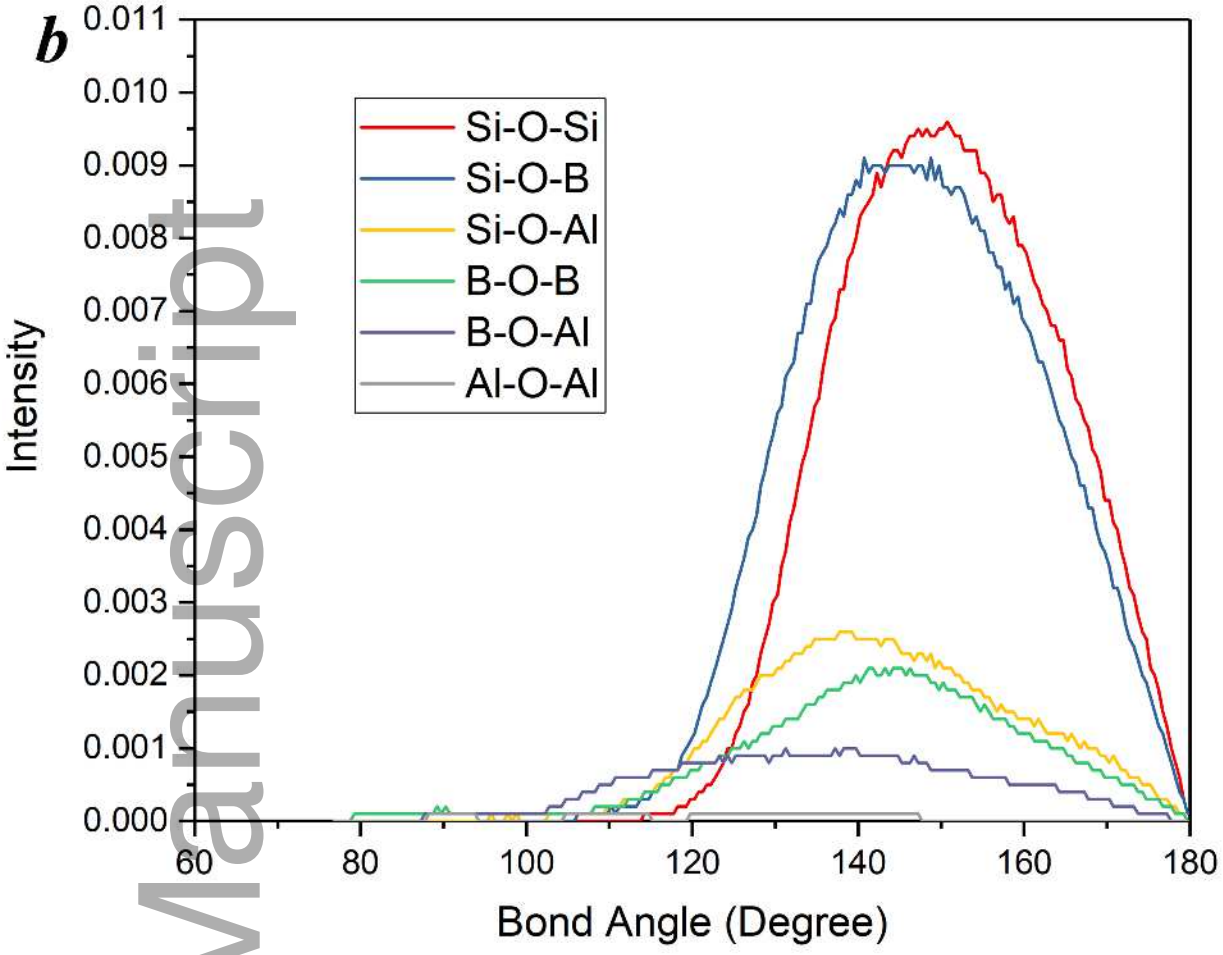

jace_16374_f5b.tif

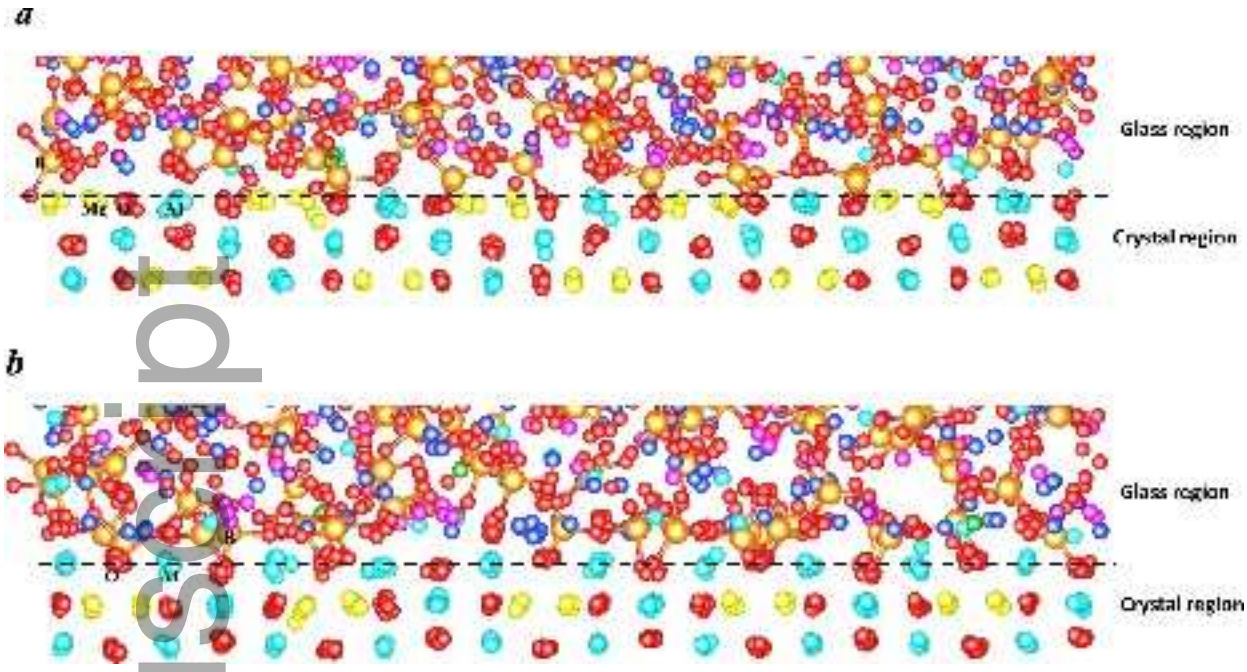

jace_16374_f6.tif

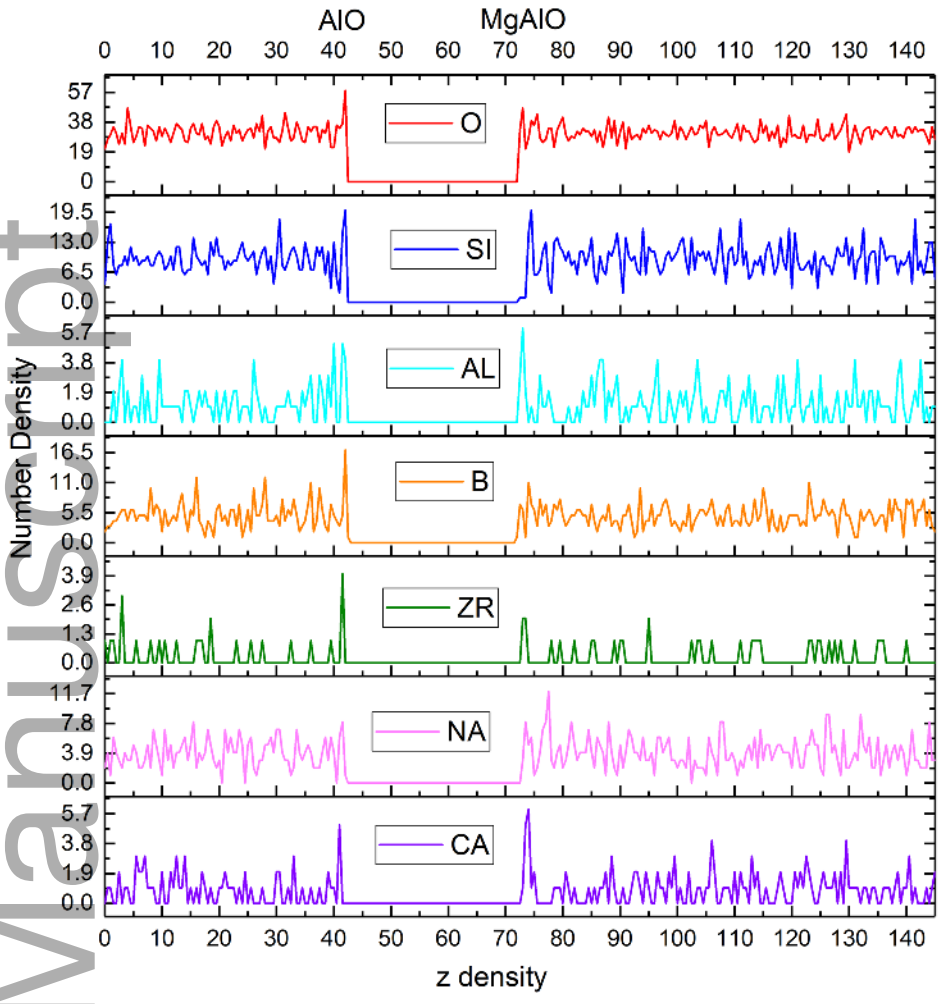

jace_16374_f7.tif

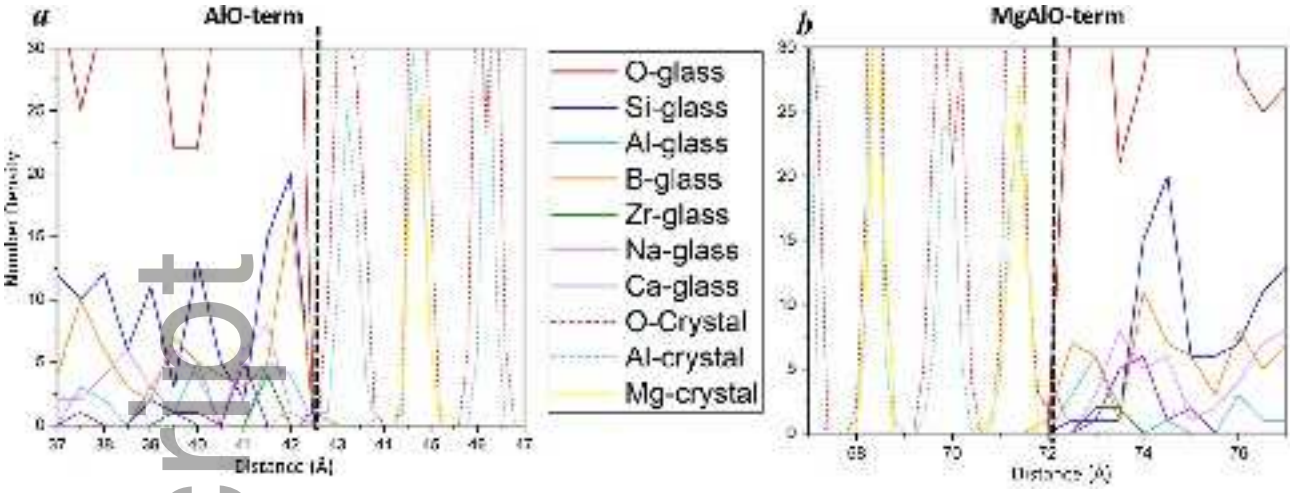

jace_16374_f8.tif

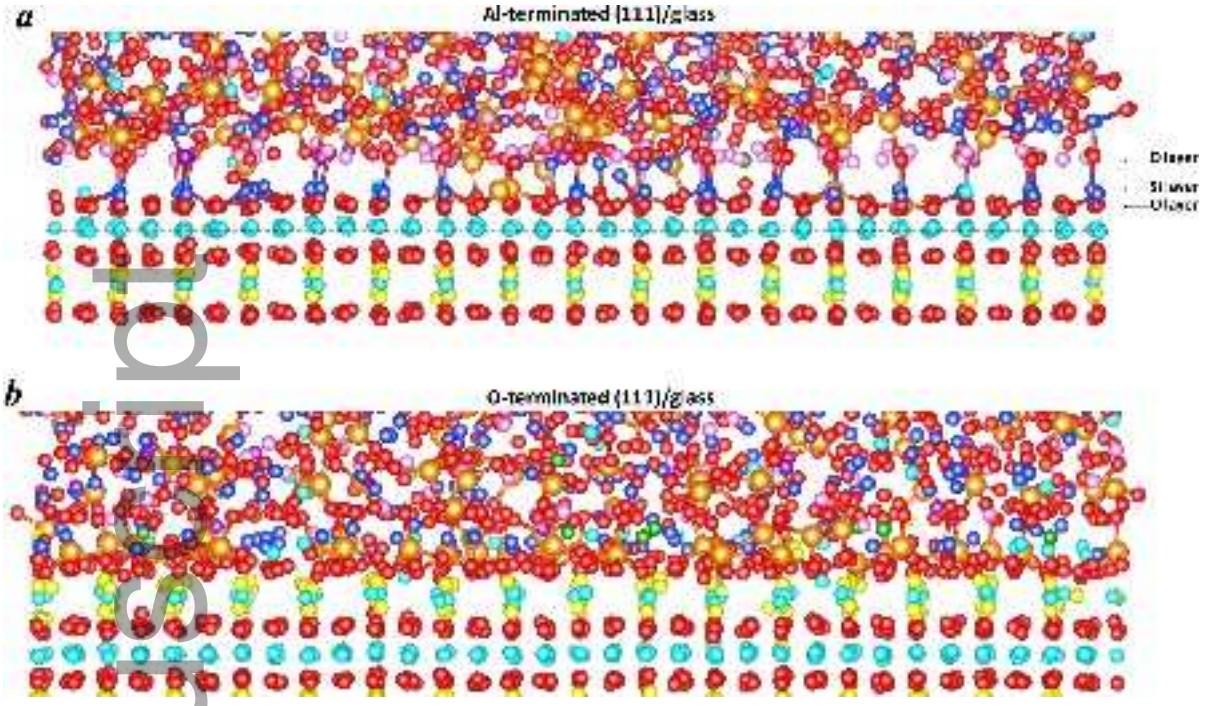

jace_16374_f9.tif